

1 **Live Imaging of SARS-CoV-2 Infection in Mice Reveals Neutralizing Antibodies Require Fc**
2 **Function for Optimal Efficacy**

3
4 Irfan Ullah^{1,#}, Jérémie Prévost^{2,3,#}, Mark S Ladinsky^{4,@}, Helen Stone^{5,@}, Maolin Lu^{5,@®}, Sai Priya
5 Anand^{2,6}, Guillaume Beaudoin-Bussièrès^{2,3}, Kelly Symmes¹, Mehdi Benlarbi², Shilei Ding²,
6 Romain Gasser^{2,3}, Corby Fink⁷, Yaozong Chen⁸, Alexandra Tauzin^{2,3}, Guillaume Goyette²,
7 Catherine Bourassa², Halima Medjahed², Matthias Mack⁹, Kunho Chung¹, Craig B Wilen¹⁰,
8 Gregory A. Dekaban^{7,13}, Jimmy D. Dikeakos⁷, Emily A. Bruce¹¹, Daniel E Kaufmann^{2,3}, Leonidas
9 Stamatatos^{12,14}, Andrew T. McGuire^{12,14,15}, Jonathan Richard^{2,3}, Marzena Pazgier⁸, Pamela J.
10 Bjorkman⁴, Walther Mothes^{5,*}, Andrés Finzi^{2,3,6,*}, Priti Kumar^{1,*} and Pradeep D. Uchil^{5,*,§}

11
12 ¹Department of Internal Medicine, Section of Infectious Diseases, Yale University School of
13 Medicine, New Haven, CT 06520, USA

14 ²Centre de Recherche du CHUM, Montreal, QC, H2X0A9, Canada

15 ³Département de Microbiologie, Infectiologie et Immunologie, Université de Montréal, Montreal,
16 QC, H2X0A9, Canada

17 ⁴Division of Biology and Biological Engineering, California Institute of Technology, Pasadena,
18 CA 91125, USA

19 ⁵Department of Microbial Pathogenesis, Yale University School of Medicine, New Haven CT
20 06510, USA

21 ⁶Department of Microbiology and Immunology, McGill University, Montreal, Qc, H3A 2B4,
22 Canada

23 ⁷Department of Microbiology and Immunology, University of Western Ontario, London, ON, N6A
24 5B7, Canada

25 ⁸Infectious Disease Division, Department of Medicine, Uniformed Services University of the
26 Health Sciences, Bethesda, MD 20814, USA

27 ⁹Universitätsklinikum Regensburg, Innere Medizin II – Nephrologie, 93042 Regensburg,
28 Germany

29 ¹⁰Departments of Laboratory Medicine and Immunobiology, Yale University School of Medicine,
30 New Haven, CT 06520, USA

31 ¹¹Division of Immunobiology, Dept. of Medicine, Larner College of Medicine, University of
32 Vermont. Burlington, VT 05405. USA.

33 ¹²Vaccine and Infectious Disease Division, Fred Hutchinson Center, Seattle, WA 98195, USA

34 ¹³Molecular Medicine Research Laboratories, Robarts Research Institute, University of Western
35 Ontario, London, ON, N6A 5B7, Canada

36 ¹⁴Department of Global Health, University of Washington, Seattle, WA 98195, USA

37 ¹⁵Department of Laboratory Medicine and Pathology, University of Washington, Seattle, WA
38 # , @ Contributed equally to the work

39 [®] Present address, Cellular and Molecular Biology, University of Texas Health Science Center at
40 Tyler TX 75708, USA

41 ***Address of correspondence to:**

42 [§]pradeep.uchil@yale.edu, priti.kumar@yale.edu, andres.finzi@umontreal.ca, -walther.mothes@
43 yale.edu

44 [§]Lead Author

45

46 **Figures: 7**

47 **Supplemental figures: 7**

48 **Supplemental Table: 1**

49 **Supplemental videos: 5**

50 **SUMMARY**

51 Neutralizing antibodies (NAbs) are effective in treating COVID-19 but the mechanism of immune
52 protection is not fully understood. Here, we applied live bioluminescence imaging (BLI) to monitor
53 the real-time effects of NAb treatment in prophylaxis and therapy of K18-hACE2 mice intranasally
54 infected with SARS-CoV-2-nanoluciferase. We could visualize virus spread sequentially from the
55 nasal cavity to the lungs and thereafter systemically to various organs including the brain, which
56 culminated in death. Highly potent NAbs from a COVID-19 convalescent subject prevented, and
57 also effectively resolved, established infection when administered within three days. In addition
58 to direct Fab-mediated neutralization, Fc effector interactions of NAbs with monocytes,
59 neutrophils and natural killer cells were required to effectively dampen inflammatory responses
60 and limit immunopathology. Our study highlights that both Fab and Fc effector functions of NAbs
61 are essential for optimal *in vivo* efficacy against SARS-CoV-2.

62

63 **Key words:** SARS-CoV-2, COVID-19, nanoluciferase, bioluminescence imaging, neutralizing
64 antibodies, convalescent patients, human ACE2 transgenic mice, monocytes, natural killer cells,
65 pathogenesis, inflammatory cytokines, Fc effector functions

66 **Introduction**

67 SARS-CoV-2-neutralizing monoclonal antibodies (NAbs) are an attractive countermeasure for
68 both COVID-19 prevention and therapy (Schafer et al., 2021; Voss et al., 2020; Weinreich et al.,
69 2021). To date, multiple NAbs against the spike (S) glycoprotein of SARS-CoV-2 have been
70 isolated from convalescent subjects. The majority of NAbs bind to the receptor binding domain
71 (RBD) in the S1 subunit and inhibit virus attachment to the human Angiotensin Converting
72 Enzyme 2 (hACE2) receptor. NAbs against the N-terminal domain (NTD) of S1 as well as the S2
73 subunit have also been isolated (Liu et al., 2020; Voss et al., 2020). NAbs have demonstrated
74 varying levels of efficacy and protection in multiple animal models of SARS-CoV-2 (Alsoussi et
75 al., 2020; Baum et al., 2020; Fagre et al., 2020; Hansen et al., 2020; Hassan et al., 2020; Li et al.,
76 2020; Rogers et al., 2020; Shi et al., 2020b; Winkler et al., 2020; Zost et al., 2020a; Zost et al.,
77 2020b). However, the *in vitro* neutralization potency of NAbs has not consistently correlated with
78 *in vivo* protection (Bournazos et al., 2014; Schafer et al., 2021). While the antigen binding domain
79 (Fab) of antibodies are critical for neutralization, the fragment crystallizable (Fc) domain can
80 contribute significantly to their *in vivo* efficacy (Bournazos et al., 2019; Bournazos et al., 2014;
81 DiLillo et al., 2014; Lu et al., 2018). Fc effector functions can also be detrimental to the host,
82 especially against respiratory viruses such as respiratory syncytial virus (RSV) and SARS-CoV-1
83 leading to antibody-dependent enhancement (ADE) and aggravated disease pathology (Bolles et
84 al., 2011; Halstead and Katzelnick, 2020; Ruckwardt et al., 2019). Therefore, a careful
85 investigation of NAb mechanisms that elicit protective or pathological consequences is required
86 prior to clinical deployment.

87 Animal models evaluated to date (Johansen et al., 2020; Leist et al., 2020a; Leist et al.,
88 2020b) have not fully recapitulated pathological features of human COVID-19. Transgenic mice
89 expressing hACE2 under the cytokeratin 18 promoter (K18-hACE2 mice) have some distinct
90 advantages. Their heightened susceptibility to human-tropic SARS-CoV-2 virus strains with

91 mortality ensuing within a week (McCray et al., 2007; Shi et al., 2020a; Winkler et al., 2020) sets
92 a high bar for identifying effective intervention strategies. In humans, SARS-CoV-2 infection
93 disables innate immunity and elicits an imbalanced inflammatory cytokine response in the lungs
94 leading to acute respiratory distress syndrome (ARDS) which is the major cause of death
95 (Graham and Baric, 2020). K18-hACE2 mice also display lung inflammation, cytokine storm and
96 impaired respiratory function (Winkler et al., 2020). However, mortality is due to neuroinvasion
97 (Carossino et al., 2021; Golden et al., 2020; Leist et al., 2020a). Interestingly, many SARS-CoV-
98 2 patients display a myriad of neurological symptoms (Ellul et al., 2020). Finally, mouse Fc γ Rs
99 display similar affinities to human antibodies (Dekkers et al., 2017). Therefore, K18-hACE2 mice
100 are excellent models for evaluating candidate human anti-SARS-CoV-2 Abs and anti-viral
101 interventions.

102 Bioluminescence imaging (BLI)-guided studies permit live visualization of pathogen
103 spread, in relevant tissues enabling real-time outcome assessments for treatment regimens. A
104 BLI-driven platform has not yet been harnessed for studying infectious respiratory pathogens like
105 SARS-CoV-2 that require level 3 biosafety containment. Here, we established a BLI-driven
106 approach to study SARS-CoV-2 infection with a well characterized replication competent SARS-
107 CoV-2 virus carrying a nanoluciferase (nLuc) reporter in the place of the ORF7A gene (Xie et al.,
108 2020a; Xie et al., 2020b). SARS-CoV-2-nLuc closely mimics the wildtype virus replication kinetics
109 and stably maintains the nLuc reporter over five generations *in vitro*. Further, ORF7a deletion was
110 recently shown not to affect pathology of the wildtype virus (Silvas et al., 2021). *In vivo* BLI
111 revealed that the virus spreads from the nasal cavity to lungs to establish infection. This is followed
112 by sequential infection of cervical lymph nodes (cLNs), brain, and finally systemic dissemination.
113 Upon neuroinvasion, the virus replicates rapidly in the brain leading to fulminant infection and
114 death by 6-7 days post infection (dpi). A single prophylactic intraperitoneal (i.p.) administration of
115 highly potent NAbs isolated from a convalescent COVID-19 subject prevented SARS-CoV-2-
116 induced mortality in K18-hACE2 mice. Protection was associated with widespread localization of

117 administered NABs and Fc-mediated effector functions with contributions from neutrophils,
118 monocytes and NK cells as well as reduced induction of inflammatory cytokines. BLI also revealed
119 a therapeutic window of 3 dpi for NAB for successfully halting progression and spread of infection
120 from the lungs. Thus, our BLI-driven study highlights that both neutralizing and Fc effector
121 functions of NABs are essential for optimal *in vivo* efficacy against SARS-CoV-2.

122

123 **Results**

124 **BLI allows Visualization of SARS-CoV-2 Replication Dynamics and Pathogenesis**

125 We tracked spread of SARS-CoV-2-nLuc using BLI after intranasal (i.n.) challenge in K18-hACE2
126 mice (**Figure 1A**). 1×10^5 FFU of SARS-CoV-2 generated sufficient photon flux to allow non-
127 invasive BLI with luciferase signal detected only in C57BL/6J (B6) mice expressing hACE2
128 (**Figure 1B**). Temporal tracking of emitted light intensities revealed that the virus replicated in the
129 nasal cavity in a biphasic manner (**Figure 1C**). Luminescent signal in the nose increased the first
130 two days of infection and diminished before increasing again between 5 to 6 dpi when systemic
131 spread occurred. The first signs of infection in the lungs were observed at 1 dpi. The nLuc signal
132 then steadily increased in until 3 dpi. nLuc signals in the cLNs and brain region were detected
133 (imaging in ventral position) at 4 dpi. A steep rise in brain nLuc activity occurred from 4 to 6 dpi
134 indicating neuroinvasion and robust virus replication (**Figure 1B, C, Video S1**). This was
135 accompanied by widespread virus replication in the gut and genital tract with loss in body weight.
136 By 6 dpi, infected K18-hACE2 mice lost 20% of their initial body weight, became moribund and
137 succumbed (**Figure 1D, E**). In contrast, as expected, B6 mice did not experience any weight loss
138 and survived the virus challenge.

139 To visualize the extent of viral spread with enhanced sensitivity and resolution, we imaged
140 individual organs after necropsy (**Figure 1B, F**). Most organs analyzed from K18-hACE2 mice
141 showed nLuc activity with maximum signal in the brain followed by the lung and nasal cavity

142 **(Figure 1F)** and mirrored the viral loads [Focus Forming Units (FFUs) and nLuc activity] measured
143 in these tissues **(Figure 1G, H)**. Real-time PCR and histology to detect hACE2 and SARS-CoV-
144 2 N confirmed widespread infection in keeping with hACE2 expression in individual tissues/organs
145 **(Table S1, Figure S1A)**.

146 Reporter-expressing viruses often purge foreign genes, particularly *in vivo*, due to fitness
147 and immune pressure (Falzarano et al., 2014; Ventura et al., 2019). The ratio of copy numbers of
148 SARS-CoV-2 nucleocapsid (N) to nLuc in the viral RNA by real-time PCR analyses of input virions
149 and virions isolated from sera of mice at 6 dpi, however, remained unchanged **(Figure 1I)**
150 indicating that the reporter was stable throughout the experimental timeline. Thus, nLuc activity
151 was a good surrogate for virus replication *in vivo*.

152 SARS-CoV-2 infection triggers an imbalanced immune response and a cytokine storm
153 that contributes substantially to pathogenesis (Del Valle et al., 2020). mRNA levels of
154 inflammatory cytokines *IL6*, *CCL2*, *CXCL10* and *IFN γ* in the lungs and brains of mice after
155 necropsy at 6 dpi were significantly upregulated in infected K18-hACE2 mice compared to B6
156 **(Figure 1J, K)**. Consistent with enhanced inflammation, we observed infiltration of Ly6G⁺
157 neutrophils and Ly6C⁺ monocytes in both lung and brain (Figure S1C). Overall, cytokine mRNAs
158 were highest in the brain with *CXCL10* mRNA copy numbers ~1000 fold higher in K18-hACE2
159 than in B6 mice corroborating extensive infection **(Figure 1J, K)**.

160 We used BLI data to pinpoint infected regions within lungs, brain, and testis for directed
161 histology and electron tomographic studies **(Figure 2)**. Higher resolution imaging revealed that
162 SARS-CoV-2 viruses were associated to large extent with capillary endothelial cell and/or alveolar
163 type-1 cells in close vicinity to alveolar macrophages in the lungs **(Figure 2A-D; Video S2, S3)**.
164 In the brain, neuronal cells (hACE2⁺MAP2⁺GFAP⁻CD68⁻CD11b⁻) were positive for SARS-CoV-2
165 N and EM tomography revealed an array of SARS-CoV-2 viruses associated within the dendrites
166 **(Figure 2E-J, Figure S1B, Video S4)**. In the testis, Sertoli cells stained positively for N **(Figure**

167 **2K-N, Video S5**). EM tomography also showed a large population of virions within pleomorphic
168 membrane-bound compartments of Sertoli cells.

169

170 **Highly Potent SARS-CoV-2 NAbs CV3-1 and CV3-25 from a Convalescent Donor**

171 We recently characterized plasma from a COVID-19 convalescent subject (S006) with
172 potent neutralizing activity and high levels of SARS-CoV-1 cross-reactive Abs (Lu et al., 2020).
173 We probed the B cell receptor (BCR) repertoire from this donor to isolate broad and potent NAbs.
174 Using recombinant SARS-CoV-2 S ectodomain (S2P) as bait for antigen-specific B cells, we
175 screened a library of S-targeted BCR clones to identify two potent NAb candidates: CV3-1 and
176 CV3-25 (Jennewein et al., 2021). We characterized their epitope specificity using ELISA, cell-
177 surface staining, virus capture assay and surface plasmon resonance (SPR) (Ding et al., 2020;
178 Prevost et al., 2020). Both NAbs recognized SARS-CoV-2 S, as a stabilized ectodomain (S-6P)
179 or when displayed on cells and virions, with low-nanomolar affinity (**Figure 3A-E**). While CV3-1
180 bound the SARS-CoV-2 RBD, CV3-25 targeted the S2 subunit (**Figure 3A, D-E**) and cross-
181 reacted with SARS-CoV-1 S on cells or virions, but not with S from other
182 human coronaviruses (**Figure 3B-C**). In agreement with the previous smFRET data for S006
183 plasma, CV3-1 stabilized S in the RBD-up (~ 0.1 FRET) conformation (**Figure 3F-H**), as seen with
184 hACE2 and most RBD-directed NAbs (Lu et al., 2020). Interestingly, CV3-25-bound S showed a
185 partial shift towards downstream conformations (~ 0.1 and ~ 0.3 FRET), suggesting a distinct
186 inhibitory mechanism from CV3-1 (**Figure 3F-H**).

187 We next measured neutralization and Fc-dependent functions of CV3-1 and CV3-25.
188 While both NAbs blocked infection by SARS-CoV-2 pseudovirus or live virus and interfered with
189 S-driven cell-to-cell fusion, CV3-1 was ~ 10 times more potent than CV3-25 (**Figure 3I-L**). To
190 evaluate Fc-mediated effector functions, we used assays that quantify the antibody-dependent
191 cellular cytotoxicity (ADCC) and antibody-dependent cellular phagocytosis (ADCP) activities.

192 CV3-1 and CV3-25 efficiently bound and eliminated S-expressing cells by stimulating cytotoxic
193 and phagocytic responses in immune effector cells (**Figure 3L-N**). Overall, both NABs displayed
194 significant neutralization and Fc-dependent antibody functions, although CV3-1 was found to be
195 more effective. The combinatorial effect of the two NABs (1:1 ratio) was similar to the response
196 with CV3-1 alone (**Figure 3I-N**).

197

198 **Prophylactic Treatment with NABs Protects K18-hACE2 Mice from SARS-CoV-2 Infection**

199 We first monitored the tissue biodistribution of Alexa Fluor 647 (AF₆₄₇) conjugated CV3-1 and
200 AF₅₉₄-conjugated CV3-25 in various tissues 24 h after i.p. delivery in mice by fluorescence
201 imaging, histology and ELISA. All three approaches revealed widespread distribution of both
202 NABs in multiple organs including the SARS-CoV-2 target tissues nasal cavity, lung and the brain
203 (**Figure S2, S3A-D**). We next tested a prophylactic regimen where each NAB was delivered i.p.
204 alone (12.5 mg/kg body weight) or in 1:1 combination (6.25 mg each NAB/kg body weight) 24 h
205 before i.n. challenge with SARS-CoV-2 nLuc (**Figure 4A**). Temporal monitoring by whole-body
206 BLI revealed that all three prophylactic regimens substantially reduced SARS-CoV-2 infection in
207 the lungs and subsequent spread (**Figure 4B-D**). Remarkably, pretreatment with CV3-1 alone or
208 in combination with CV3-25 (cocktail 1:1) produced near complete protection from SARS-CoV-2
209 infection with no signals detected in most organs by live non-invasive imaging or after terminal
210 necropsy at 22 dpi (**Figure 4B-D, G, H**). Moreover, all test cohorts survived with no discernible
211 weight loss, nLuc activity or viral loads signifying complete control of virus infection (**Figure 4E-**
212 **I**). In CV3-25-pretreated animals, lung infection and subsequent neuroinvasion occurred at
213 reduced intensity, and was also reflected in individual organs after necropsy (**Figure 4B, G, H**).
214 CV3-25 delayed mortality by ~2 days in 4 out of the 6 animals and viral loads in the nasal cavity,
215 lungs, and brain at the time of necropsy (8 dpi) were similar to that in the control cohorts treated
216 with isotype-matched antibodies at 6 dpi (**Figure 4F, I**).

217 Pre-treatment with CV3-1 or NAb cocktail also prevented the inflammatory cytokine
218 induction (**Figure 4J, K**). In contrast, heightened levels of cytokine mRNA were detected in mice
219 that had succumbed to infection in control as well as in CV3-25 cohorts (**Figure 4J, K**). Mice that
220 survived in the CV3-25 cohorts, regained body weight and at 22 dpi, had no detectable virus in
221 organs and base-line inflammatory cytokine induction (**Figure 4E-K**). Overall, our data indicated
222 that CV3-1 alone, was sufficient to inhibit establishment of virus infection and prophylactically
223 protect K18-hACE2 mice. Histology of brain tissue revealed that NAb CV3-1 and CV3-25
224 persisted even at 6 dpi (**Figure S3E**). However, while CV3-1 localization remained unaltered post-
225 infection due to the absence of viral neuroinvasion in this cohort, CV3-25 localized heavily onto
226 the surface of infected neurons at 6 dpi, consistent with virus infection in the brain (**Figure S3E**).
227 Additionally, neutrophils infiltrated the brain in mice treated with CV3-25 alone (**Figure S3F**).
228 These data, together with the imaging analyses indicated that CV3-1 inhibited virus dissemination
229 rather than neutralizing virus in peripheral tissues. In *in vivo* dose response studies, just 0.75 mg
230 CV3-1/kg body weight was sufficient to afford 50% efficacy against lethal SARS-CoV-2 infection
231 (**Figure S4**). These data indicated that CV3-1 is highly potent at halting SARS-CoV-2 at early
232 infection sites and was primarily responsible for protecting the cohort treated with the NAb
233 cocktail.

234 **CV3-1 Therapy Rescues Mice from Lethal SARS-CoV-2 Infection**

235 We explored if CV3-1 could also cure mice infected with SARS-CoV-2-nLuc. Mice were
236 administered CV3-1 at 1, 3, and 4 dpi after confirming SARS-CoV-2 infection was established in
237 the lungs (**Figure 5A**). Temporal imaging and quantification of nLuc signal revealed that CV3-1,
238 administered at 1 and 3 dpi, controlled virus spread successfully preventing neuroinvasion
239 (**Figure 5B-D, G, H**). This was corroborated by the absence of weight loss and/or recuperation of
240 body weight, undetectable viral loads, and near-baseline levels of inflammatory cytokines in
241 tissues (**Figure 5E-K**). CV3-1 therapy at 4 dpi, however, could neither control virus spread nor
242 neuroinvasion resulting in 75% mortality of the cohort (**Figure 5B-F**) with loss in body weight, high

243 inflammatory cytokines levels and tissue viral loads, similar to the control cohort (**Figure 5E-K**).
244 Thus, the therapeutic window for maximal efficacy of CV3-1 treatment extends for up to 3 days
245 from the initiation of SARS-CoV-2 infection.

246

247 **CV3-1 and CV3-25 Require Antibody Effector Functions For *In vivo* Efficacy**

248 Antibodies may also mediate Fc-recruitment of immune cells to eliminate infected cells (Lu et al.,
249 2018). We explored a role for Fc-mediated effector functions in the *in vivo* protection afforded by
250 NAbs. We generated mutant versions with Leucine to Alanine (L234A/L235A, LALA) changes of
251 both NAbs to impair interaction with Fc receptors (Saunders, 2019) and a
252 G236A/S239D/A330L/I332E (GASDALIE) version of CV3-25 known to enhance affinity to Fc γ Rs.
253 (Bournazos et al., 2014). LALA and GASDALIE mutations had no impact on S binding and
254 neutralizing capabilities of NAbs (**Figure S5A, B**). As expected, LALA mutations compromised
255 ADCC and ADCP activities whereas CV3-25 GASDALIE displayed enhanced ADCC activity
256 (**Figure S5C, D**). Biodistribution analyses of AF₆₄₇-conjugated mutants of CV3-1, CV3-25 24h
257 after i.p. administration revealed penetration into most tissues (**Figure S5E**).

258 We next tested the impact of Fc-effector altering mutations on the prophylactic efficacy of
259 NAbs (**Figure S6A**). Longitudinal non-invasive BLI and terminal imaging analyses after necropsy,
260 body weight changes, survival and viral load estimations revealed that LALA mutations had
261 indeed compromised efficacy of both antibodies (**Figure S6A-I**). SARS-CoV-2 replicated better,
262 invaded the brain and induced body weight loss in cohorts treated with LALA NAbs compared to
263 the corresponding wildtype NAbs (**Figure S6D-E**). Histology at 6 dpi revealed that both LALA
264 NAbs had penetrated the brain tissue during the course of infection and bound the surface of
265 infected neurons (**Figure S5F, G**). At 6 dpi, both the CV3-1 LALA and CV3-25 LALA cohorts had
266 higher tissue viral loads compared to the respective wildtype cohorts indicating compromised
267 protective efficacy (**Figure S6G**). Similarly, while tissue viral loads in CV3-25-pretreated mice
268 were reduced by a log, those in CV3-25 LALA-pretreated mice were comparable to that in control

269 cohorts. The delayed mortality and 25% protective efficacy offered by CV3-25 was abrogated and
270 the protective efficacy of CV3-1 fell from 100% to 62.5% with the corresponding LALA mutants
271 **(Figure S6F)**. There was also an overall increase in the inflammatory cytokine signature in the
272 LALA cohorts **(Figure S6H, I)**. The requirement for Fc effector function for CV3-1 prophylaxis was
273 surprising as no infection was detected in CV3-1-pretreated mice both by non-invasive and post-
274 necropsy tissue imaging at 6 dpi **(Figure 4)**. However, examination of tissues at 3 dpi did reveal
275 weak nLuc signals in the nasal cavity and lungs despite absence of signal by non-invasive imaging
276 **(Figure S5H-M)**. PCR analyses also confirmed the presence SARS-CoV-2 N RNA in these
277 tissues at 3 dpi **(Figure S5M)**. Thus, some incoming viruses managed to establish infection
278 despite CV3-1 prophylaxis and Fc effector functions were required to eliminate infected cells.
279 Correspondingly, Fc-effector enhanced CV3-25 GASDALIE reduced virus dissemination and
280 provided 100% protective efficacy despite a transient loss in body weight in mice compared to the
281 wild-type CV3-25 **(Figure S6B-F)**. Viral titers and inflammatory cytokines were also significantly
282 reduced compared to control cohorts **(Figure S6G-I)**. We also tested the requirement for Fc-
283 effector functions using mouse-adapted SARS-CoV-2 MA10 in WT B6 mice (Dinnon et al., 2020;
284 Leist et al., 2020), an alternative model where mice succumb due to ARDS. CV3-1 successfully
285 neutralized SARS-CoV-2 MA10 with similar efficacies to the WA1 strain *in vitro* ($IC_{50} = 0.01837$
286 $\mu\text{g/mL}$). Though we had to use 5-fold more virus and older B6 mice (12-14 weeks) to induce
287 mortality, we observed a similar Fc effector requirement for CV3-1 to prophylactically protect mice
288 and reduce viral loads and inflammation in lung and brain **(Figure S6J-O)**. The requirement for
289 Fc-effector function for CV3-1 prophylaxis suggested that the same should be critical for CV3-1
290 therapy **(Figure 6A)**. Indeed, while CV3-1 treatment at 3 dpi controlled infection, cohorts treated
291 with CV3-1 LALA displayed rapidly spreading lung infection and fully succumbed by 6 dpi after an
292 accelerated loss in body weight **(Figure 6B-F)**. High viral loads and cytokine levels in tissues also
293 reflected the failure of the LALA NAbS to treat pre-established viral infection **(Figure 6G)**. Notably,
294 while the lung viral loads in CV3-1 LALA cohorts were similar to that in the control, inflammatory

295 cytokine mRNA levels in lungs, *CXCL10* in particular, were significantly higher suggesting a
296 crucial requirement for Fc-engagement in curbing a cytokine-storm like phenotype (**Figure 6H-I**).

297

298 **Monocytes, Neutrophils and Natural Killer (NK) cells Contribute to Antibody-mediated** 299 **Effector Functions *In Vivo***

300 Fc can recruit NK cells, monocytes, or neutrophils to facilitate clearance of infected cells and
301 shape the cytokine response produced by these cells for enhancing adaptive and cell-mediated
302 immune responses (Lu et al., 2018). When NK cells were depleted prior to CV3-1 prophylaxis
303 (**Figure S7J, K**), weak nLuc signals appeared in lungs of infected mice; however, this did not
304 progress to the levels seen in control cohorts with no CV3-1 treatment (**Figure S7A-D**). They also
305 experienced a temporary but significant decrease in body weight (**Figure S7E**). Nevertheless, NK
306 cell depletion did not decrease the survival statistics of CV3-1 prophylaxis and all the mice
307 survived despite marginal increases in viral loads in target organs and significant increases in
308 inflammatory cytokine levels (**Figure S7F-K**). Thus, while NK cells do contribute to *in vivo* efficacy
309 of CV3-1, their absence did not compromise the protection offered by CV3-1 prophylaxis.

310 In therapeutic regimen format, when CV3-1 treatment was initiated at 3 dpi (**Figure 7A**),
311 depleting NK cells compromised protective efficacy with 25% of the mice succumbing to SARS-
312 CoV-2 infection compared to a 100% survival rate of mice cohorts replete with NK cells (**Figure**
313 **7B-F, S7J, K**). Depleting Ly6G⁺ neutrophils and Ly6C^{hi} CD11b⁺ classical monocytes under CV3-
314 1 therapy. resulted in 75% and 80% of the mouse cohorts respectively failing to control SARS-
315 CoV-2 spread, with loss in body weight resulting in death (**Figure 7A-G, S7L-O**) (Mack et al.,
316 2001). This was accompanied by increased viral burden and enhanced expression of *CCL2*,
317 *CXCL10*, and *Il6* mRNA in target tissues (**Figure 7H-J**). Overall, neutrophils, monocytes and NK
318 cells contributed to the antibody-dependent cure of mice from lethal SARS-CoV-2 infection and
319 were critical for the success of SARS-CoV-2 NAb-directed therapies.

320 In summary, our data demonstrate the utility of a BLI-guided platform for temporo-spatial
321 visualization of SARS-CoV-2 replication, pathogenesis and the mechanisms contributing to an
322 effective outcome with NAb-based interventions in K18-ACE2 mice.

323

324 **Discussion**

325 NAb therapies are being explored to augment current vaccination strategies against
326 SARS-CoV-2 to expand the protection afforded towards emerging variants of concern. However,
327 prior evidence for antibody-dependent enhancement of pathology caused by respiratory viruses
328 like RSV and SARS-CoV-1 warrants careful investigation of antibody effects *in vivo* before clinical
329 implementation (Iwasaki and Yang, 2020; Klasse and Moore, 2020). We have established a
330 whole-body imaging approach to follow the dynamics and pathogenesis of SARS-CoV-2 infection
331 in mice to facilitate preclinical studies for identifying effective therapeutic measures against
332 COVID-19. Temporal tracking revealed that SARS-CoV-2 first replicates in the nasal cavity,
333 reaches the lungs at 1 dpi where the infection expands till 3 dpi before spreading systemically to
334 other organs including the brain at 4 dpi. BLI also helped illuminate how the highly potent human
335 NAb CV3-1 (targets Spike RBD) and CV3-25 (binds S2 domain) differed in their ability to protect
336 or treat SARS-CoV-2 infection in the highly susceptible K18-hACE2 mouse model. Imaging
337 analyses revealed widespread distribution of NAb within the animals, including in the nasal cavity
338 and lungs where the virus infection is initially established, and persistence for at least a week after
339 administration, features that were critical for efficacy in this acute model for SARS-CoV-2. BLI
340 also revealed a therapeutic window of 3 dpi for CV3-1 NAb to successfully halt progression of
341 infection from lungs to distal tissues. As previously reported SARS-CoV-2 NAb have a
342 therapeutic window of 1 dpi (Alsoussi et al., 2020; Hassan et al., 2020; Schafer et al., 2021;
343 Winkler et al., 2021), CV3-1 displays one of the most potent *in vivo* efficacy profiles with a broad
344 therapeutic window till 3 dpi. Most protective human NAb for SARS-CoV-2 tested in animal

345 models and in humans, target RBD (Baum et al., 2020; Chen et al., 2021; Rogers et al., 2020;
346 Schafer et al., 2021; Tortorici et al., 2020; Weinreich et al., 2021), some NTD targeting NABs have
347 also display potent antiviral activity *in vivo* (Li et al., 2021; Noy-Porat et al., 2021; Voss et al.,
348 2020). We show that the S2-directed CV3-25 NAb also conferred protection, albeit not as potently
349 as CV3-1. This of significance as newly emerging variants display fewer mutations in the S2
350 subunit compared to the S1. Indeed, CV3-25 can efficiently neutralize the B.1.351 variant, while
351 neutralization by anti-NTD and anti-RBD NABs was greatly diminished (Stamatatos et al., 2021)
352 Hence epitopes in S2 targeted by CV3-25 can be explored to generate future antigenic templates
353 for potent pan-coronavirus antibodies (Sauer et al., 2021).

354 Our data also establishes that neutralizing capacity of NABs alone is insufficient to garner
355 clinical protection. LALA variants of CV3-1 revealed a crucial role for Fc-mediated interactions in
356 augmenting *in vivo* protection not only for therapy, but also in prophylaxis in contrast to a recent
357 report where Fc-effector was involved only during NAb therapy (Winkler et al., 2021). CV3-1 Fc
358 effector functions were needed to eliminate infected cells originating from viruses that eluded
359 neutralization during prophylaxis in both the B6 mouse model with mouse-adapted SARS-CoV-2
360 MA10 and in K18-hACE2. However, in agreement with previous study (Winkler et al., 2021),
361 diminishing Fc function of CV3-1 completely compromised its ability to therapeutically cure mice.
362 Surprisingly, body weight loss and inflammatory responses (CCL2, CXCL10, IFN γ) were
363 aggravated in mice administered CV3-1 LALA therapeutically compared to control cohorts. Thus,
364 the Fc region plays an additional protective role in limiting immunopathology by dampening
365 inflammatory responses. A previously reported NAb engaged only monocytes for *in vivo* activity
366 (Winkler et al., 2021). In contrast, CV3-1 engaged Fc-interacting neutrophils, monocytes and NK
367 cells for its *in vivo* efficacy. Thus, in addition to potent neutralizing activity, effective engagement
368 of innate immune components contributed to the high *in vivo* potency of CV3-1.

369 CV3-1, at low doses, did not enhance infection but displayed protective efficacy of only
370 50%. Thus, our data add to the growing body of evidence suggesting absence of an ADE

371 mechanism during SARS-CoV-2 infection with a protective rather than pathogenic role for Fc
372 (Schafer et al., 2021; Winkler et al., 2021). However, as the expression pattern of murine Fc γ Rs
373 on immune cells differs from that in humans, additional investigations, in other animal models, are
374 required to confirm definitive absence of ADE in SARS-CoV-2 infection (Gorman et al., 2021).
375 Moreover, elucidation of the major Fc γ R(s) (Fc γ RI, Fc γ RIII and/or Fc γ RIV) engaged by NAbS will
376 help design ultrapotent SARS-CoV-2 Nab therapies (Smith et al., 2012). Here we have taken a
377 step in this direction by introducing GASDALIE mutations to augment Fc γ R interactions and
378 enhance *in vivo* potency of CV3-25.

379 In summary, our study demonstrates the utility of the BLI-guided approach to study SARS-
380 CoV-2 pathogenesis and identify effective antiviral therapies for rapid translation to clinical use in
381 humans.

382

383 **Supplemental information**

384 7 Supplementary figures, 1 table and 5 Videos

385 **Author contributions**

386 Conceptualization, PDU, PK, AF, WM, IU and JP; Methodology, PDU, IU, JP, MSL, ML.WM, AF,
387 PK; Investigation, IU, PDU, JP, HS, KS, LS, ATM, SPA, GBB, MB, SD, RG, CF, YC, AT, GG, CB,
388 HM, GAD, JDD, DEK, JR, MP; Writing – Original Draft, PDU; Writing – Review & Editing, PDU,
389 PK, AF, WM, IU, JP, LS, ATM; Funding Acquisition, AF, LS, ATM, PJB; Resources, AF, PJB,
390 CBW, MM; Supervision, PDU, WM, PK, AF, PJB.

391

392 **Acknowledgements**

393 This work was supported by George Mason University Fast Grants to MSL and PJB;
394 P20GM125498 (awarded to UVM Translational Global Infectious Disease Research Center) to

395 EAB; le Ministère de l'Économie et de l'Innovation du Québec, Programme
396 de soutien aux organismes de recherche et d'innovation, Fondation du CHUM, Canadian
397 Institutes of Health Research (CIHR) foundation grant #352417 & Rapid Research Funding
398 Opportunity #FRN440388 to JDD and G.A.D, Canada Research Chair on Retroviral Entry no.
399 RCHS0235 950-232424 to AF; Canada's COVID-19 Immunity Task Force (CITF) & Canada
400 Foundation for Innovation (CFI) #41027 to AF and DEK & #36287 to JDD. and GAD; FRQS Merit
401 Research Scholarship to DEK; CIHR fellowships to JP, SPA and GBB,
402 MITACS Accélération postdoctoral fellowship to RG; Fred Hutch COVID-19 Research Fund to LS
403 and ATM.

404

405 **Disclaimer**

406 The views expressed in this presentation are those of the authors and do not reflect the official
407 policy or position of the Uniformed Services University, US Army, the Department of Defense, or
408 the US Government.

409

410 **Declaration of Interests**

411 The authors declare no competing interests.

412 **Figure Legends**

413 **Figure 1. Visualization of SARS-CoV-2 Replication Dynamics in hACE2 Transgenic Mice**

414 (A) Experimental strategy utilizing SARS-CoV-2 carrying nLuc reporter in ORF7a for non-invasive
415 BLI of virus spread following intranasal (i.n.) challenge of B6 or K18-hACE2 mice.

416 (B) Representative images from temporal BLI of SARS-CoV-2-nLuc-infected mice in ventral (v)
417 and dorsal (d) positions at the indicated dpi and after necropsy

418 (C) Temporal quantification of nLuc signal as flux (photons/sec) acquired non-invasively in the
419 indicated tissues of each animal. The color bar above the x-axis (yellow to orange) represents
420 computed signal intensities in K18-hACE2 mice that are significantly above those in B6 mice.

421 (D) Temporal changes in mouse body weight with initial body weight set to 100%.

422 (E) Kaplan-Meier survival curves of mice for experiment as in A statistically compared by log-rank
423 (Mantel-Cox) test.

424 (F) *Ex vivo* imaging of indicated organs and quantification of nLuc signal as flux(photons/sec) at
425 6 dpi after necropsy.

426 (G, H) Viral loads (FFUs/mg or nLuc activity/mg) in indicated tissue measured on Vero E6 cells
427 as targets. Non-detectable virus amounts were set to 1.

428 (I) Ratio of C_t values for SARS-CoV-2 nucleocapsid (N) and nLuc estimated by RT-PCR using
429 RNA extracted from input virions (inoculum) and virions from sera of mice at 6 dpi.

430 (J, K) Fold changes in cytokine mRNA levels in lung and brain tissues at 6 dpi after normalization
431 to *GAPDH* mRNA in the same sample and that in uninfected mice.

432 Each curve in (C) and (D) and each data point in (F), (I), (J), and (K) represents an individual
433 mouse. Scale bars in (B and (F) denote radiance (photons/sec/cm²/steradian). *p* values obtained
434 by non-parametric Mann-Whitney test for pairwise comparison. *, *p* < 0.05; **, *p* < 0.01; ***, *p* <
435 0.001; ****, *p* < 0.0001; ns, not significant; Mean values ± SD are depicted.

436

437 **Figure 2. EM localization of SARS-CoV-2 Virions in Lung, Brain and Testis of Infected K18-**

438 **hACE2 Mice**

439 (A) 2D overview of a lung region featuring red blood cells (rbc) within a pulmonary capillary, an
440 alveolar Type 2 cell (AT2).

441 (B) Slice from a 3D tomogram of square region in A showing membrane-enclosed cytoplasmic
442 compartments (arrowheads) containing presumptive SARS-CoV-2 virions in capillary endothelial
443 cells.

444 (C) Presumptive virions from tomogram in B displayed at equatorial views. Presumptive virions
445 were identified as described in *Methods* and are directly comparable to those in SARS-CoV-2
446 infected Vero-E6 cells (panels O-Q).

447 (D) ImmunoEM tomography of presumptive SARS-CoV-2 virions from infected lung tissue,
448 labeled with antiserum against Spike protein and gold (10 nm) conjugated secondary antibodies.
449 Gold particles localized to the outer peripheries of virions indicate specific labeling of SARS-CoV-
450 2 Spikes.

451 (E) Tomography of SARS-CoV-2 infected brain tissue. Presumptive SARS-CoV-2 virions (red
452 arrowheads) are present within a neuron (pale green). A dendritic synaptic terminal to the left of
453 the virus-containing neuron shows that presumptive SARS-CoV-2 virions are easily distinguished
454 from typical synaptic neurotransmitter vesicles.

455 (F) 2D overview of brain tissue illustrating the complex spatial relationship among neurons and
456 other brain cell types. Presumptive SARS-CoV-2 virions are present in two compartments (black
457 squares) within a single neuron.

458 (G, H) Tomographic slices of black squares in F. Presumptive SARS-CoV-2 virions (red
459 arrowheads) appear to be aligned within compartments that border the edges of a neural
460 projection.

461 (I) Presumptive SARS-CoV-2 virions from tomograms in G and H.

462 (J) ImmunoEM tomography as in D of presumptive SARS-CoV-2 virions from infected brain tissue.

463 (K) (Upper) BLI of testis from a SARS-CoV-2 infected mouse to identify infected regions for IF
464 and EM analyses. (Lower) IF image of an infected testis region stained with antibodies to SARS-
465 CoV-2 Nucleocapsid (red)
466 (L) 2D overview of testis corresponding to region of high intensity (red) in the upper panel of K,
467 showing Sertoli cells surrounded by developing sperm (left) and one primary spermatocyte (1°S,
468 upper right). Presumptive SARS-CoV-2 virions are localized to membrane-bound compartments
469 in Sertoli cells (black squares).
470 (M, N) Slices from two 3D tomograms of squares in L. Presumptive SARS-CoV-2 virions
471 (arrowheads) are present within membrane-enclosed cytoplasmic compartments. These
472 compartments contain additional structures amongst the discernable SARS-CoV-2 virions
473 (insets).
474 (O) EM localization of virions in SARS-CoV-2 infected Vero-E6 cells, processed for EM as above
475 tissue samples. Virions were characterized (see Methods) and compared to presumptive virions
476 in the tissue samples to confidently verify their identities. 2D overview of infected Vero-E6 cell in
477 a 150 nm section.
478 (P) Tomogram of rectangle in O showing >100 presumptive SARS-CoV-2 virions contained within
479 cytoplasmic exit compartments.
480 (Q) Virions from the tomogram in P showing common features of dense RNC puncta, discernable
481 surface spikes, vary in size (~60-120 nm) and shape. Virions are directly comparable to those
482 shown for the tissue samples in C and I.
483 Scale bar length for each image is shown at the bottom.

484

485 **Figure 3. *In vitro* Characterization of CV3-1 and CV3-25 NABs**

486 (A) NAb binding to SARS-CoV-2 Spike ectodomain (S-6P) or RBD estimated by ELISA. Relative
487 light units (RLU) were normalized to the cross-reactive SARS-CoV-1 mAb CR3022. NAb binding

488 to SARS-CoV-2 S2 N-His tag protein on cell-surface of transfected 293T cells analyzed by flow
489 cytometry. Median fluorescence intensities (MFIs) for anti-Spike NABs were normalized to the
490 signal obtained with an anti-His tag mAb.

491 (B) Flow cytometric detection of 293T cells expressing S from the indicated human CoVs. MFI
492 from 293T cells transfected with empty vector was used for normalization.

493 (C) Pseudoviruses bearing SARS-CoV-2 or SARS-CoV-1 S were tested for capture by anti-
494 Spike NABs. The cross-reactive CR3022 mAb was used for normalization.

495 (D-E) NAb binding affinity and kinetics to SARS-CoV-2 S using Surface Plasmon Resonance
496 (SPR). SARS-CoV-2 S-6P or S2 ectodomain was immobilized as the ligand on the chip and CV3-
497 1 or CV3-25 Fab was used as analyte at concentrations ranging from 1.56 to 100 nM for both
498 Fabs to S-6P and 3.125nM to 200nM for CV3-25 to S2 (2-fold serial dilution, see Methods for
499 details). Alternatively, CV3-1 IgG was immobilized on the chip and SARS-CoV-2 RBD used as
500 analyte from 1.56 to 50 nM (2-fold serial dilution). Kinetic constants were determined using a 1:1
501 Langmuir model in BIA evaluation software (experimental readings depicted in blue and fitted
502 curves in black).

503 (F-H) FRET histograms of ligand-free S on S-MEN coronavirus-like particles (VLPs) or in
504 presence of 50 µg/mL of CV3-1 (G) or CV3-25 (H). VLPs were incubated for 1 h at 37°C before
505 smFRET imaging. N_m is the number of individual FRET traces compiled into a conformation-
506 population FRET histogram (gray lines) and fitted into a 4-state Gaussian distribution (solid black)
507 centered at 0.1-FRET (dashed cyan), 0.3-FRET (dashed red), 0.5-FRET (dashed green), and 0.8-
508 FRET (dashed magenta).

509 (I) Neutralizing activity of CV3-1 and CV3-25 alone or in combination (1:1 ratio) on SARS-CoV-2
510 S bearing pseudoviruses using 293T-ACE2 cells.

511 (J) Microneutralization activity of anti-Spike NABs on live SARS-CoV-2 virus using Vero E6 cells.

512 (K) Inhibition of cell-to-cell fusion between 293T cells expressing HIV-1 Tat and SARS-CoV-2 S
513 and TZM-bl-ACE2 cells by NABs.

514 Half maximal inhibitory antibody concentration (IC_{50}) values in I-K were determined by normalized
515 non-linear regression analyses.

516 (L) MFI of CEM.NKr cells expressing SARS-CoV-2 Spike (CEM.NKr-Spike) stained with indicated
517 amounts of NABs and normalized to parental CEM.NKr.

518 (M) % ADCC in the presence of titrated amounts of NABs using 1:1 ratio of parental CEM.NKr
519 cells and CEM.NKr-Spike cells as targets when PBMCs from non-infected donors were used as
520 effector cells

521 (N) % ADCP in the presence of titrated amounts of NABs using CEM.NKr-Spike cells as targets
522 and THP-1 cells as phagocytic cells.

523

524 **Figure 4. Prophylactic Treatment with CV3-1 Protects Mice from Lethal SARS-CoV-2**
525 **Infection**

526 (A) Experimental design to test *in vivo* efficacy of NABs CV3-1 and CV3-25 administered alone
527 (12.5 mg/kg body weight) or as a 1:1 cocktail (6.25 mg/kg body weight each) 1 day prior to
528 challenging K18-hACE2 mice (i.n.) with SARS-CoV-2-nLuc followed by non-invasive BLI every 2
529 days. Human IgG1-treated (12.5 mg/kg body weight) mice were the control cohort (Iso).

530 (B) Representative BLI images of SARS-CoV-2-nLuc-infected mice in ventral (v) and dorsal (d)
531 positions.

532 (C-D) Temporal quantification of nLuc signal as flux (photons/sec) computed non-invasively.

533 (E) Temporal changes in mouse body weight with initial body weight set to 100%.

534 (F) Kaplan-Meier survival curves of mice statistically compared by log-rank (Mantel-Cox) test.

535 (G, H) *Ex-vivo* images of organs and nLuc signal quantified as flux (photons/sec) after necropsy.

536 (I) Viral loads (nLuc activity/mg tissue) measured in Vero E6 cells as targets. Non-detectable virus
537 amounts were set to 1.

538 (J, K) Fold changes in cytokine mRNA levels in lung and brain tissues normalized to *GAPDH*
539 mRNA in the same sample and that in non-infected mice after necropsy.

540 Viral loads (I) and inflammatory cytokine profile (J, K) were determined after necropsy for mice
541 that succumbed to infection at 6dpi and in mice surviving at 22 dpi.
542 Scale bars in (B) and (G) denote radiance (photons/sec/cm²/steradian). Each curve in (C)-(E) and
543 each data point in (H)-(K) represents an individual mouse. Grouped data in (C)-(K) were analyzed
544 by 2-way ANOVA followed by Dunnett's or Tukey's multiple comparison tests. Statistical
545 significance for group comparisons to isotype control are shown in black and for those to CV3-25
546 are shown in red. *, p < 0.05; **, p < 0.01; ***, p < 0.001; ****, p < 0.0001; Mean values ± SD
547 are depicted.

548

549 **Figure 5. CV3-1 Therapy Protects Mice from Lethal SARS-CoV-2 Infection**

550 (A) Experimental design to test *in vivo* efficacy of CV3-1 administered i.p. (12.5 mg/kg body
551 weight) at indicated times after i.n. challenge of K18-hACE2 mice with SARS-CoV-2 nLuc followed
552 by non-invasive BLI every 2 days. Human IgG1 treated (12.5 mg/kg body weight) mice were the
553 control cohort (Iso).

554 (B) Representative images from temporal BLI of SARS-CoV-2-nLuc-infected mice in ventral (v)
555 and dorsal (d) positions. Scale bars denote radiance (photons/sec/cm²/steradian).

556 (C-D) Temporal quantification of nLuc signal as flux (photons/sec) computed non-invasively.

557 (E) Temporal changes in mouse body weight with initial body weight set to 100%.

558 (F) Kaplan-Meier survival curves of mice statistically compared by log-rank (Mantel-Cox) test.

559 (G, H) *Ex vivo* imaging of organs and quantification of nLuc signal as flux(photons/sec) after
560 necropsy.

561 (I) Viral loads (nLuc activity/mg tissue) measured in Vero E6 cells as targets. Non-detectable virus
562 amounts were set to 1.

563 (J, K) Fold changes in cytokine mRNA levels in lung and brain tissues normalized to GAPDH
564 mRNA in the same sample and that in non-infected mice after necropsy.

565 Viral loads (I) and inflammatory cytokine profile (J, K) were determined after necropsy at 6dpi.
566 Each curve in (C)-(E) and each data point in (H)-(K) represents an individual mouse. CV3-1
567 treatment times are indicated in (C)-(E). Grouped data in (C)-(K) were analyzed by 2-way ANOVA
568 followed by Dunnett's or Tukey's multiple comparison tests. Statistical significance for group
569 comparisons to isotype control are shown in black and for groups under CV3-1 therapies to 4 dpi-
570 treatment shown in red. *, $p < 0.05$; **, $p < 0.01$; ***, $p < 0.001$; ****, $p < 0.0001$; Mean values \pm
571 SD are depicted.

572

573 **Figure 6. Fc-mediated Antibody Effector Functions Contribute to the *In Vivo* Efficacy of**
574 **CV3-1**

575 (A) Experimental design to test therapeutic efficacy of NAb CV3-1 and its corresponding Leucine
576 to Alanine (LALA) mutant administered ip (12.5 mg/kg body weight) in K18-hACE2 mice 3 dpi with
577 SARS-CoV-2 nLuc followed by non-invasive BLI every 2 days. Human IgG1-treated (12.5 mg/kg
578 body weight) mice were used as the control cohort (Iso).

579 (B) Representative images from temporal BLI of SARS-CoV-2-nLuc-infected mice in ventral (v)
580 and dorsal (d) positions. Scale bars denote radiance (photons/sec/cm²/steradian).

581 (C-D) Temporal quantification of nLuc signal as flux (photons/sec) computed non-invasively.

582 (E) Temporal changes in mouse body weight with initial body weight set to 100%.

583 (F) Kaplan-Meier survival curves of mice statistically compared by log-rank (Mantel-Cox) test.

584 (G) Viral loads (nLuc activity/mg tissue) measured in Vero E6 cells as targets. Non-detectable
585 virus amounts were set to 1.

586 (H, I) Fold changes in cytokine mRNA levels in lung and brain tissues normalized to *Gapdh* mRNA
587 in the same sample and that in non-infected mice after necropsy.

588 Viral loads (G) and inflammatory cytokine profile (H, I) were determined after necropsy at 6dpi.
589 Each curve in (C)-(E) and each data point in (G)-(I) represents an individual mouse. CV3-1
590 treatment times are indicated in (C)-(E). Grouped data in (C)-(I) were analyzed by 2-way ANOVA

591 followed by Dunnett's or Tukey's multiple comparison tests. Statistical significance for group
592 comparisons to isotype control are shown in black and between CV3-1 and CV3-1 LALA treated
593 cohorts are shown in red. *, $p < 0.05$; **, $p < 0.01$; ***, $p < 0.001$; ****, $p < 0.0001$; Mean values
594 \pm SD are depicted.

595

596 **Figure 7. Monocytes, Neutrophils and Natural Killer Cells Contribute to Antibody Effector**
597 **Functions *In Vivo***

598 (A) Experimental design to test the contribution of NK cells, neutrophils (CD11b⁺Ly6G⁺) and
599 monocytes (CCR2⁺Ly6^{hi} CD11b⁺) in K18-hACE2 mice therapeutically treated with CV3-1 NAb
600 (i.p., 12.5 mg/kg body weight) at 3 dpi after challenge with SARS-CoV-2-nLuc. α NK1.1, α Ly6G
601 and α CCR2 mAbs (i.p., 20, 20 and 2.5 mg/kg body weight respectively) were used to deplete NK
602 cells, neutrophils and monocytes respectively every 48h starting at 1 dpi. Human and/or rat
603 isotype mAb treated cohorts served as controls (Iso). The mice were followed by non-invasive
604 BLI every 2 days from the start of infection.

605 (B) Representative images from temporal BLI of SARS-CoV-2-nLuc-infected mice in ventral (v)
606 and dorsal (d) positions. Scale bars denote radiance (photons/sec/cm²/steradian).

607 (C-D) Temporal quantification of nLuc signal as flux (photons/sec) computed non-invasively.

608 (E) Temporal changes in mouse body weight with initial body weight set to 100%.

609 (F) Kaplan-Meier survival curves of mice statistically compared by log-rank (Mantel-Cox) test.

610 (H) Viral loads (nLuc activity/mg tissue) measured in Vero E6 cells as targets. Non-detectable
611 virus amounts were set to 1.

612 (I, J) Fold change in cytokine mRNA levels in lung and brain tissues normalized to *GAPDH* mRNA
613 in the same sample and that in non-infected mice after necropsy.

614 Viral loads (H) and inflammatory cytokine profile (I, J) were determined after necropsy at 6dpi.

615 Each curve in C-E and each data point in H-J represents an individual mouse.

616 Grouped data in (C)-(I) were analyzed by 2-way ANOVA followed by Dunnett's or Tukey's multiple
617 comparison tests. Statistical significance: group comparisons to isotype control are shown in
618 black; group comparisons to Iso+CV3-1 within the NK and neutrophil depleted cohorts are shown
619 in purple; group comparisons to Iso+CV3-1 within the monocyte-depleted cohorts are shown in
620 red. *, $p < 0.05$; **, $p < 0.01$; ***, $p < 0.001$; ****, $p < 0.0001$; Mean values \pm SD are depicted.
621

622 STAR Methods

623 KEY RESOURCES TABLE

REAGENT or RESOURCE	SOURCE	IDENTIFIER
Antibodies		
Fc block anti mouse-CD16/CD32 (93)	BioLegend Inc	Cat # 101302 RRID: AB_312801
PE/Cy7 anti-mouse CD3(17A2)	BioLegend Inc	Cat # 100219 RRID: AB_1732068
PE anti-mouse CD11b (M1/70)	BioLegend Inc	Cat # 101207 RRID: AB_312790
APC/Cy7 anti-mouse Ly-6C (HK1.4)	BioLegend Inc	Cat #128025 RRID: AB_10643867
APC anti-mouse NK-1.1 (PK136)	BioLegend Inc	Cat # 108709 RRID: AB_313396
Alexa Fluor® 488 anti-mouse Ly-6G (Clone 1A8)	BioLegend Inc	Cat # 127626 RRID: AB_2561340
Alexa Fluor® 647 anti-mouse Ly-6C (Clone HK1.4)	BioLegend Inc	Cat # 128010 RRID: AB_1236550
APC Rat anti-mouse CD45 (30-F11)	BD-Pharmingen	Cat # 559864 RRID:AB_398672
Anti-CCR2 (clone MC-21) for monocyte depletion	(Mack et al., 2001)	Matthias.Mack@klinik.uni-regensburg.de
InVivoMAb anti-mouse LY6G (clone: 1A8) for neutrophil depletion	Bio X Cell	Cat # BE0075-1 RRID: AB_1107721
InVivoMAb rat IgG2b isotype control, clone LTF-2 for monocyte depletion	Bio X Cell	Cat # BE0090 RRID: AB_1107780
InVivoMAb anti-mouse NK1.1 (clone PK136)	Bio X Cell	Cat # BE0036 RRID: AB_1107737
InVivoMab rat IgG2a clone C1.18.4; Isotype controls for NK and neutrophil depletion	Bio X Cell	Cat # BE0085 RRID: AB_1107771
InVivoMAb human IgG1 isotype control	Bio X Cell	Cat # BE0297 RRID: AB_2687817
Cross-reactive SARS-CoV-1 monoclonal antibody CR3022	(ter Meulen et al., 2006)	RRID: AB_2848080

CV3-1	Finzi Lab, Université de Montréal	(Jennewein et al., 2021)
CV3-25	Finzi Lab, Université de Montréal	(Jennewein et al., 2021)
CV3-1 LALA	Finzi Lab, Université de Montréal	N/A
CV3-25 LALA	Finzi Lab, Université de Montréal	N/A
CV3-25 GASDALIE	Finzi Lab, Université de Montréal	N/A
Mouse monoclonal anti-polyHistidine antibody	Sigma-Aldrich	Cat # H1029; RRID: AB_260015
Goat anti-Human IgG (H+L) Cross-Adsorbed Secondary Antibody, Alexa Fluor 647	Invitrogen	Cat # A-21445; RRID: AB_2535862
Goat anti-Mouse IgG (H+L) Cross-Adsorbed Secondary Antibody, Alexa Fluor 647	Invitrogen	Cat # A-21235; RRID: AB_2535804
Goat anti-Human IgG Fc Cross-Adsorbed Secondary Antibody, HRP	Invitrogen	Cat # A18823; RRID: AB_2535600
Mouse anti-SARS-CoV-2 nucleocapsid (clone 1C7)	Bioss Antibodies	Cat # bsm-41411M
Alexa Fluor® 647 anti-MAP2 Antibody (clone SMI 52)	BioLegend Inc	Cat # 801806 RRID: AB_2721422
Alexa Fluor® 488 anti-GFAP Antibody (clone 2E1.E9)	BioLegend Inc	Cat # 644704 RRID: AB_2566109
Alexa Fluor® 594 anti-mouse CD68 Antibody (clone FA-11)	BioLegend Inc	Cat # 137020 RRID: AB_2563305
Alexa Fluor® 488 anti-mouse/human CD11b Antibody (clone M1/70)	Biolegend Inc	Cat # 101219 RRID: AB_493545
Rabbit anti-SARS-CoV-2 nucleocapsid	Novus	Cat # NB100-56576
Rabbit anti-human ACE2 polyclonal antibody	Sigma-Aldrich	Cat # HPA000288
Bacterial and Virus Strains		
SARS-CoV-2-nLuc (strain 2019-nCoV/USA_WA1/2020)	Craig B Wilen (Yale University)	K. Plante and Pei-Yong Shi, World Reference Center for Emerging Viruses and Arboviruses, University of Texas Medical Branch)
SARS-CoV-2 USA-WA1/2020	BEI resources	Cat # NR-52281
SARS-CoV-2-MA10 (mouse-adapted virus)	Craig B Wilen (Yale University)	Ralph Baric, UNC, School of Medicine (Dinnon et al., 2020; Leist et al., 2020a)

Biological Samples		
Primary human peripheral blood mononuclear cells (PBMCs)	FRQS AIDS network	N/A
Chemicals, Peptides, and Recombinant Proteins		
Liberase TL Research Grade	Sigma-Aldrich	Cat# 5401020001
DNAse I recombinant, RNAse-free	Roche	Ref # 04716728001
Gibco™ RPMI 1640 medium	Thermo Fisher Scientific	Cat # 11875093
Gibco™ Dulbecco's modified Eagle's medium (DMEM)	Thermo Fisher Scientific	Cat # 11965118
Gibco™ MEM Non-essential amino acid (NEAA) solution	Thermo Fisher Scientific	Cat # 11140050
Gibco™ Penicillin-streptomycin solution (10,000 U/ml)	Thermo Fisher Scientific	Cat # 15140122
Gibco™ Dulbecco's Phosphate Buffered Saline (DPBS)	Thermo Fisher Scientific	Cat # 14190144
Gibco™ L-Glutamine (200mM)	Thermo Fisher Scientific	Cat # 25030081
Gibco™ 0.05% Trypsin-EDTA, phenol red	Thermo Fisher Scientific	Cat # 25300054
Fetal bovine serum	Atlanta Biologicals	Cat # S11550
RBC Lysis Buffer (10X)	BioLegend Inc	Cat # 420301
Bovine Serum Albumin (BSA)	Sigma-Aldrich	Cat# A9647-100G CAS: 9048-46-8
Accutase	BioLegend Inc	Cat # 423201
0.05% Trypsin-EDTA (1X)	Life Technologies	Cat # 25300-054
K3 EDTA 15% Solution	Fisher Scientific	Cat # BD 366450
Sodium pyruvate (100 mM)	Life technologies	Ref # 11360-070
2-Mercaptoethanol	Sigma-Aldrich	Cat # M3148
L-Glutamine (200mM)	Life technologies	Ref # 25030-081
Red blood cell lysis buffer-Hybri-Max	Sigma-Aldrich	Cat # R7757-100ML
Tris-buffered saline (TBS)	Thermo Fisher Scientific	Cat # BP24711
Western Lightning Plus-ECL, Enhanced Chemiluminescence Substrate	Perkin Elmer Life Sciences	Cat # NEL105001EA
Tween20	Thermo Fisher Scientific	Cat # BP337-500
Passive lysis buffer	Promega	Cat # E1941

Triton-X 100 t-octyl phenoxy polyethoxyethanol	American Bioanalytical	Cat # AB02025-00500 CAS: 9002-93-1
Paraformaldehyde (PFA)	Electron Microscopy Sciences	Cat # 19200 CAS: 30525-89-4
Rat serum	Stemcell Biotechnologies	Cat # 13551
L-lysine Monohydrochloride	Sigma-Aldrich	Cat # L1262
Sodium (meta)periodate	Sigma-Aldrich	Cat # 30323-100G CAS: 7790-28-5
Sucrose/ α -D-glucopyranosyl- β -D-fructofuranoside	americanBIO	Ref # AB01900-01000 CAS: 57-50-1
Tissue-Tek O.C.T Compound	Sakura	Cat # 4583
Fc receptor blocker	Innovex	Cat # NB335-5
Superforst® Plus microscope slides	Thermo Scientific	Cat # 4951PLUS-001
Glutaraldehyde	Electron Microscopy Sciences	Cat # 16220 CAS: 111-30-8
Sodium cacodylate trihydrate	Electron Microscopy Sciences	Cat #12300
Osmium tetroxide	Electron Microscopy Sciences	Cat #19110
Uranyl acetate	Electron Microscopy Sciences	Cat #22400
Acetone, EM-Grade, Glass-Distilled	Electron Microscopy Sciences	Cat #10015
Epon-Araldite resin	Electron Microscopy Sciences	Cat #13940
Lead citrate	Electron Microscopy Sciences	Cat #17800 CAS: 512-26-5
Gold beads (10 nm)	Ted Pella, Inc.	Cat. #15703-1
Dimethyl sulfoxide (DMSO)	Sigma-Aldrich	Cat # D2650-5X5ML CAS: 67-68-5
Sodium azide	Sigma-Aldrich	Cat # S-8032 EC No: 247-852-1
Sodium phosphate, Monobasic, Monohydrate, Crystal (NaH ₂ PO ₄ ·H ₂ O)	J.T.Baker	Cat # 3818-01 CAS: 10049-21-5

Sodium phosphate, Dibasic, Anhydrous (Na ₂ HPO ₄)	J.T.Baker	Cat # 3828-01 CAS: 7558-79-4
Glycine	American Bioanalytical	Cat # AB00730-01000 CAS: 56-40-6
The PEG-it Virus precipitation solution (5X)	System Bioscience	Cat # LV810A-1
Avicel® Pharma Grade	FMC	Cat # RC-581 NF 10.20944/preprints202005.0264.v1
Vector® TrueView® Autofluorescence Quenching Kit	Vector Laboratories	SP-8400
Puromycin dihydrochloride	Millipore Sigma	Cat # P8833
D-Luciferin potassium salt	Thermo Fisher Scientific	Cat # L2916
Formaldehyde 37%	Thermo Fisher Scientific	Cat # F79-500
LIVE/DEAD Fixable AquaVivid Cell Stain	Thermo Fisher Scientific	Cat # L34957
Cell proliferation dye eFluor670	Thermo Fisher Scientific	Cat # 65-0840-85
Cell proliferation dye eFluor450	Thermo Fisher Scientific	Cat # 65-0842-85
FreeStyle 293F expression medium	ThermoFisher Scientific	Cat # 12338002
ExpiFectamine 293 transfection reagent	ThermoFisher Scientific	Cat # A14525
Protein A Sepharose CL-4B	Cytiva	Cat # 17096303
Ni-NTA agarose	Invitrogen	Cat # R90110
Papain-agarose resin	ThermoFisher Scientific	Cat # 20341
SARS-CoV-2 S2 ectodomain C-His tag protein	BEI Resources	NR-53799
SIGMAFAST OPD	EMD Millipore	Cat # P9187
Critical Commercial Assays		
Nano-Glo Luciferase Assay System (nanoluc substrate)	Promega	Cat # N1120
Pierce™ Gaussia Luciferase Glow Assay Kit	ThermoFisher Scientific	Cat # 16160
Mix-n-Stain CF 647 Antibody Labeling Kit (50-100µg)	Sigma-Aldrich	Cat # MX647S100 SIGMA
Mix-n-Stain CF 488A Antibody Labeling Kit (50-100µg)	Sigma-Aldrich	Cat # MX488AS100 SIGMA
Alexa Fluor 594 Protein Labeling Kit	Invitrogen	Cat # A10239

Alexa Fluor 647 Protein Labeling Kit	Invitrogen	Cat # A20173
Strep-Tactin®XT 4Flow	IBA Lifesciences	Cat # 2-5998-000
KAPA SYBR FAST qPCR Master Mix (2X) Kit	KAPA Biosystems	Cat # KK4600 and KK4601
Ambion DNase I (RNase-free)	ThermoFisher Scientific	Cat # AM2222
RNeasy Mini Kit (50)	Qiagen	Cat #/ID 74104
iScript advanced cDNA kit	Bio Rad	Cat #1725038
iQ Multiplex Powermix	Bio Rad	Cat # 1725848
iScript™ cDNA Synthesis Kit	Bio Rad	Cat # 95047-100
Deposited Data		
Experimental Models: Cell Lines		
Vero E6	ATCC	Cat # CRL-1586; RRID: CVCL_0574
Vero E6-TMPRSS2	Craig B. Wilen	Yale University
HEK293	ATCC	Cat # CRL-1573; RRID: CVCL_0045
HEK293T	ATCC	Cat # CRL-3216; RRID: CVCL_0063
Expi293F cells	ThermoFisher Scientific	Cat # A14527
293T-ACE2	(Prevost et al., 2020)	N/A
Cf2Th	ATCC	Cat # CRL-1430; RRID: CVCL_3363
CEM.NKr-CCR5+	NIH AIDS Reagent Program	Cat # 4376; RRID: CVCL_X623
CEM.NKr-Spike	(Anand et al., 2021a)	N/A
TZM-bl	NIH AIDS Reagent Program	Cat # 8129; RRID: CVCL_B478
TZM-bl-ACE2	This paper	N/A
THP-1	ATCC	Cat # TIB-202; RRID: CVCL_0006
FreeStyle 293F cells	ThermoFisher Scientific	Cat # R79007; RRID: CVCL_D603
Experimental Models: Organisms/Strains		
C57BL/6J (B6)	The Jackson Laboratory	The Jackson Laboratory Stock No: 000664 RRID: IMSR_JAX:000664

B6.Cg-Tg(K18-ACE2)2PrImn/J	The Jackson Laboratory	Stock No: 034860 RRID:IMSR_JAX:034860
Oligonucleotides		
SARS-CoV-2 N F: 5'-ATGCTGCAATCGTGCTACAA-3'	Yale School of Medicine, W. M. Keck Foundation, Oligo Synthesis Resource	
SARS-CoV-2 N R: 5'-GACTGCCGCCTCTGCTC-3'	Yale School of Medicine, W. M. Keck Foundation, Oligo Synthesis Resource	
Human IgG1 L234A-L235A F: 5'-CAGCACCTGAAGCCGCGGGGGACCGTC-3'	Integrated DNA Technologies	N/A
Human IgG1 L234A-L235A R: 5'-GACGGTCCCCCGCGGCTTCAGGTGCTG-3'	Integrated DNA Technologies	N/A
Human IgG1 G236A-S239D F: 5'-CTCCTGGCGGGACCGGATGTCTTCCTCTTC-3'	Integrated DNA Technologies	N/A
Human IgG1 G236A-S239D R: 5'-GAAGAGGAAGACATCCGGTCCCGCCAGGAG-3'	Integrated DNA Technologies	N/A
Human IgG1 A330L-I332E F: 5'-GCCCTCCCACTCCCGAAGAGAAAACCATC-3'	Integrated DNA Technologies	N/A
Human IgG1 A330L-I332E R: 5'-GATGGTTTTCTCTTCGGGGAGTGGGAGGGC-3'	Integrated DNA Technologies	N/A
FAM-Gapdh	Bio Rad	Cat # 12001950
HEX-IL6	Bio Rad	Cat # 10031228
TEX615-CCL2	Bio Rad	Cat # 10031234
Cy5-CXCL10	Bio Rad	Cat # 10031231
Cy5.5-IFN γ	Bio Rad	Cat # 10031237
Transgene Forward: GAC CCC TGA GGG TTT CAT ATA G	Yale School of Medicine, W. M. Keck Foundation, Oligo Synthesis Resource	#53437, Genotyping primers for K18-hACE2 mice. The Jackson Laboratory
Common: CAC CAA CAC AGT TTC CCA AC	Yale School of Medicine, W. M. Keck Foundation, Oligo Synthesis Resource	#53438, Genotyping primers for K18-hACE2 mice. The Jackson Laboratory
Wildtype forward: AAG TTG GAG AAG ATG CTG AAA GA	Yale School of Medicine, W. M. Keck Foundation, Oligo Synthesis Resource	#53439, Genotyping primers for K18-hACE2 mice. The Jackson Laboratory

Recombinant DNA		
pCMV-SARS-CoV-2 Spike D614G Δ19	This paper	N/A
pCMV-SARS-CoV-2 Spike	Sino Biological	Cat # VG40589-UT
pDNA3.1-Ngene	(Zhang et al., 2020)	N/A
pDNA3.1-Egene	(Zhang et al., 2020)	N/A
pDNA3.1-Mgene	(Zhang et al., 2020)	N/A
pCMV delta R8.2	Addgene	Cat #12263
HIV-1-inGluc	Mothes Lab, Yale University	N/A
pLVX-M	Dr. Nevan Krogan	N/A
pLVX-E	Dr. Nevan Krogan	N/A
pLVX-N	Dr. Nevan Krogan	N/A
pCG1-SARS-CoV-2 Spike	(Hoffmann et al., 2020)	N/A
pCG1-SARS-CoV-1 Spike	(Hoffmann et al., 2013)	N/A
pCAGGS-229E Spike	(Hofmann et al., 2005)	N/A
pCAGGS-NL63 Spike	(Hofmann et al., 2005)	N/A
pCAGGS-OC43 Spike	(Prevost et al., 2020)	N/A
pCMV3-HKU1 Spike	Sino Biological	Cat # VG40021-UT
pcDNA3.1-MERS-CoV Spike	(Park et al., 2016)	N/A
paH-SARS-CoV-2 Spike HexaPro	Dr Jason S. McLellan, University of Texas	N/A
pcDNA3.1-SARS-CoV-2 RBD	(Beaudoin-Bussieres et al., 2020)	N/A
pCMV3-SARS-CoV-2 S2 N-His tag	Sino Biological	Cat # VG40590-NH
pNL4.3 R-E- Luc	NIH AIDS Reagent Program	Cat # 3418
pSVCMV-IN-VSV-G	Lodge et al.	N/A
Lentiviral packaging plasmids (pLP1, pLP2)	(Liu et al., 2013)	N/A
pLenti-C-mGFP-P2A-Puro-ACE2	OriGene	Cat # RC208442L4
pIRES2-eGFP vector	Clontech	Cat # 6029-1
pLTR-Tat	(Finzi et al., 2010)	N/A
Software and Algorithms		
Accuri CSampler software	BD Biosciences	
FlowJo v10	Treestar	https://www.flowjo.com/ RRID:SCR_008520

Nikon-Elements AR Analysis v4.13 and Acquisition v4.5	Nikon	
Adobe Photoshop CC	Adobe Systems Inc	RRID:SCR_014199
Adobe Illustrator CC	Adobe Systems Inc	RRID:SCR_010279
BioRender (schematics in figures)	BioRender.com	RRID:SCR_018361
CFX Maestro™ Software (qPCR analyses)	Bio-rad Inc	See RRID:SCR_018064
Graphpad Prism v9.0.1	GraphPad Software	https://www.graphpad.com/ RRID:SCR_002798
SerialEM software package	David N. Mastronarde, University of Colorado Boulder	https://bio3d.colorado.edu/SerialEM/
IMOD software package	David N. Mastronarde, University of Colorado Boulder	https://bio3d.colorado.edu/imod/ RRID: SCR_003297
Chimera	University of California, San Francisco	http://plato.cgl.ucsf.edu/chimera RRID: SCR_004097
Gen5 microplate reader and imager software	Biotek	RRID:SCR_017317
BIAevaluation software	GE Healthcare	Cat # BR-1005-97 RRID:SCR_015936
Other		
TriStar LB 941 Multimode Microplate Reader and Luminometer	BERTHOLD TECHNOLOGIES GmbH & Co. KG	Mothes and Finzi Lab
BD Biosciences C6 Accuri Flow Cytometer,	BD Biosciences	Yale, MMPATH, Central Facility RRID:SCR_019591
BD LSR II Flow Cytometer	BD Biosciences	https://medicine.yale.edu/immunology/flowcore/
Leica Cryostat CM1950	Leica	CM1950 (Iwasaki Lab; Yale University) RRID:SCR_018061
Nikon W1 Spinning Disk Confocal microscope	Nikon Instruments Inc, Americas	Yale West Campus Imaging Core
HPM-010 high-pressure freezing machine	Bal-Tec/ABRA, Switzerland	N/A
AFS-2 freeze-substitution machine	Leica Microsystems	N/A
Stereo dissecting microscope	Nikon Instruments Inc, Americas	Model SMZ645

UC6 ultramicrotome	Leica Microsystems	RRID:SCR_020226
Transmission electron microscope	ThermoFisher Scientific	Tecnai T12-G2 (Caltech)
2k x 2k CCD camera	Gatan, Inc	XP1000
C1000 Touch thermal cycler	Bio-Rad	RRID:SCR_019688
CFX Connect™ Real-Time PCR Detection System	Bio-Rad	RRID:SCR_018064
Nanodrop Spectrophotometer ND-1000	ThermoFisher Scientific	RRID:SCR_016517
27G × ½" insulin syringe with needle	TERUMO	Cat # SS*05M2713
31G insulin syringe	BD Biosciences	Cat # 328468
70 µm Nylon cell strainer	FALCON	Cat # 352350
Acrodisc 25 mm Syringe Filter w/0.45 µm HT Tuffryn Membrane	PALL Life Sciences	Cat # 4184
Superfrost Plus Microscope Slides	Thermo Scientific	Cat # 4951PLUS-001
96-well white plates for luciferase assays	Costar	Cat # 3917
Accu-Edge High Profile Microtome Blades	SAKURA	Cat # 4685
Microcover glasses 1 ounce No.1	VWR	Cat # 48393 106
Tissue-Tek Cryomold	SAKURA	Ref # 4557
Brass planchettes	Ted Pella, Inc.	Type A and Type B
Cryotubes	Thermo Scientific Nunc	Cat # 340711
Teflon-coated glass microscope slides		
Microsurgical scalpel	Electron Microscopy Sciences	Cat # 72047-15
Plastic sectioning stubs	Home Made	
Diamond knife	Diatome, Ltd	
Formvar-coated copper-rhodium slot grids	Electron Microscopy Sciences	
Dual-axis tomography holder	E.A. Fischione Instruments, Export PA	Model 2040
Polystyrene Round-bottom Tube	FALCON	Ref # 352058
Optical Flat 8-Cap Strips for 0.2 ml tube stripes/plates	Bio-Rad	Cat # TCS0803
Individual PCR tubes 8-tube Strip, clear	Bio-Rad	Cat # TLS0801
ThermalGrid Rigid Strip PCR tubes	Denville Scientific INC	Ref # C18064
96 well U bottom plate	FALCON	Ref # 353077
XIC-3 animal isolation chamber	PerkinElmer	

Perkin Elmer IVIS Spectrum In-Vivo Imaging System	PerkinElmer	Yale University ABSL-3 facility. RRID:SCR_018621
RAS-4 Rodent Anesthesia System	PerkinElmer	CLS146737
QUANTIFOIL® holey carbon grids	Electron Microscopy Sciences	Cat # Q250-CR1
Synergy LX multi-mode reader	Biotek	RRID:SCR_019763
Superose 6 10/300 GL	GE Healthcare	Cat # 17517201
Hiload 16/600 Superdex 200pg	GE Healthcare	Cat # 28989335
Biacore 3000	GE Healthcare	RRID:SCR_019954
Protein A sensor chip	Cytiva	Cat # 29127558
Ni-NTA sensor chip	Cytiva	Cat # BR100034

624

625 **RESOURCE AVAILABILITY**

626 **Lead Contact:** Pradeep Uchil (Pradeep.uchil@yale.edu)

627 Requests for resources and reagents should be directed to and will be fulfilled by the Lead
628 Contact, Pradeep Uchil (pradeep.uchil@yale.edu), Priti Kumar (priti.kumar@yale.edu), Andrés
629 Finzi (andres.finzi@umontreal.ca) and Walther Mothes(walther.mothes@yale.edu).

630 **Materials Availability**

631 All other unique reagents generated in this study are available from the corresponding authors
632 with a completed Materials Transfer Agreement.

633 **Data and Code Availability**

634 All the data that support the findings of this study are available from the corresponding authors
635 upon reasonable request.

636

637 **EXPERIMENTAL MODEL AND SUBJECT DETAILS**

638

639 **Cell and Viruses**

640 Vero E6 (CRL-1586, American Type Culture Collection (ATCC), were cultured at 37°C in RPMI
641 supplemented with 10% fetal bovine serum (FBS), 10 mM HEPES pH 7.3, 1 mM sodium pyruvate,
642 1× non-essential amino acids, and 100 U/ml of penicillin–streptomycin. The 2019n-
643 CoV/USA_WA1/2019 isolate of SARS-CoV-2 expressing nanoluciferase was obtained from Craig
644 B Wilen, Yale University and generously provided by K. Plante and Pei-Yong Shi, World
645 Reference Center for Emerging Viruses and Arboviruses, University of Texas Medical Branch)
646 (Xie et al., 2020a; Xie et al., 2020b). Mouse-adapted SARS-CoV-2 MA10 was obtained from Craig

647 B. Wilen, Yale University and generously provided by Ralph S Baric, Department of Epidemiology,
648 University of North Carolina at Chapel Hill (Leist et al., 2020). The SARS-CoV-2 USA-WA1/2020
649 virus strain used for microneutralization assay was obtained through BEI Resources. Viruses
650 (WA1 or MA10) were propagated in Vero-E6 or Vero E6 TMPRSS2 by infecting them in
651 T150 cm² flasks at a MOI of 0.1. The culture supernatants were collected after 72 h when
652 cytopathic effects were clearly visible. The cell debris was removed by centrifugation and filtered
653 through 0.45-micron filter to generate virus stocks. Viruses were concentrated by adding one
654 volume of cold (4 °C) 4x PEG-it Virus Precipitation Solution (40 % (w/v) PEG-8000 and 1.2 M
655 NaCl; System Biosciences) to three volumes of virus-containing supernatant. The solution was
656 mixed by inverting the tubes several times and then incubated at 4 °C overnight. The precipitated
657 virus was harvested by centrifugation at 1,500 × g for 60 minutes at 4 °C. The concentrated virus
658 was then resuspended in PBS then aliquoted for storage at -80°C. All work with infectious SARS-
659 CoV-2 was performed in Institutional Biosafety Committee approved BSL3 and A-BSL3 facilities
660 at Yale University School of Medicine or the University of Western Ontario using appropriate
661 positive pressure air respirators and protective equipment. CEM.NKr, CEM.NKr-Spike, THP-1 and
662 peripheral blood mononuclear cells (PBMCs) were maintained at 37°C under 5% CO₂ in RPMI
663 media, supplemented with 10% FBS and 100 U/mL penicillin/ streptomycin. 293T (or HEK293T),
664 293T-ACE2, CF2Th, TZM-bl and TZM-bl-ACE2 cells were maintained at 37°C under 5% CO₂ in
665 DMEM media, supplemented with 5 % FBS and 100 U/mL penicillin/ streptomycin. CEM.NKr (NIH
666 AIDS Reagent Program) is a T lymphocytic cell line resistant to NK cell-mediated lysis. CEM.NKr-
667 Spike stably expressing SARS-CoV-2 Spike were used as target cells in ADCC and ADCP assays
668 (Anand et al., 2021a). THP-1 monocytic cell line (ATCC) was used as effector cells in the ADCP
669 assay. PBMCs were obtained from healthy donor through leukapheresis and were used as
670 effector cells in ADCC assay. 293T cells (obtained from ATCC) were derived from 293 cells, into
671 which the simian virus 40 T-antigen was inserted. 293T-ACE2 cells stably expressing human
672 ACE2 is derived from 293T cells (Prevost et al., 2020). Cf2Th cells (obtained from ATCC) are
673 SARS-CoV-2-resistant canine thymocytes and were used in the virus capture assay. TZM-bl (NIH
674 AIDS Reagent Program) were derived from HeLa cells and were engineered to contain the Tat-
675 responsive firefly luciferase reporter gene. For the generation of TZM-bl cells stably expressing
676 human ACE2, transgenic lentiviruses were produced in 293T using a third-generation lentiviral
677 vector system. Briefly, 293T cells were co-transfected with two packaging plasmids (pLP1 and
678 pLP2), an envelope plasmid (pSVCMV-IN-VSV-G) and a lentiviral transfer plasmid coding for
679 human ACE2 (pLenti-C-mGFP-P2A-Puro-ACE2) (OriGene). Forty-eight hours post-transfection,
680 supernatant containing lentiviral particles was used to infect TZM-bl cells in presence of 5 µg/mL

681 of polybrene. Stably transduced cells were enriched upon puromycin selection. T2M-bl-ACE2
682 cells were then cultured in medium supplemented with 2 mg/mL of puromycin (Millipore Sigma).

683

684 **Ethics statement**

685 PBMCs from healthy individuals as a source of effector cells in our ADCC assay were obtained
686 under CRCHUM institutional review board (protocol #19.381). Research adhered to the standards
687 indicated by the Declaration of Helsinki. All participants were adults and provided informed written
688 consent prior to enrollment in accordance with Institutional Review Board approval.

689

690 **Antibodies**

691 The human antibodies (CV3-1 and CV3-25) used in the work were isolated from blood of male
692 convalescent donor S006 (male) recovered 41 days after symptoms onset using fluorescent
693 recombinant stabilized Spike ectodomains (S2P) as probes to identify antigen-specific B cells as
694 previously described (Lu et al., 2020; Seydoux et al., 2020; Jennewein et al., 2021). Site-directed
695 mutagenesis was performed on plasmids expressing CV3-1 and CV3-25 antibody heavy chains
696 in order to introduce the LALA mutations (L234A/L235A) or the GASDALIE mutations
697 (G236A/S239D/A330L/I332E) using the QuickChange II XL site-directed mutagenesis protocol
698 (Stratagene).

699

700 **Mouse Experiments**

701 All experiments were approved by the Institutional Animal Care and Use Committees (IACUC) of
702 and Institutional Biosafety Committee of Yale University (IBSCYU). All the animals were housed
703 under specific pathogen-free conditions in the facilities provided and supported by Yale Animal
704 Resources Center (YARC). All IVIS imaging, blood draw and virus inoculation experiments were
705 done under anesthesia using regulated flow of isoflurane:oxygen mix to minimize pain and
706 discomfort to the animals.

707 C57BL/6 (B6), hACE2 transgenic B6 mice (heterozygous) were obtained from Jackson
708 Laboratory. 6–8-week-old male and female mice were used for all the experiments. The
709 heterozygous mice were crossed and genotyped to select heterozygous mice for experiments by
710 using the primer sets recommended by Jackson Laboratory.

711

712 **METHOD DETAILS**

713

714 **SARS-CoV-2 infection and treatment conditions**

715 For all *in vivo* experiments, the 6 to 8 weeks male and female mice were intranasally challenged
716 with 1×10^5 FFU in 25-30 μ l volume under anesthesia (0.5 - 5 % isoflurane delivered using
717 precision Dräger vaporizer with oxygen flow rate of 1 L/min). For mouse-adapted SARS-CoV-2
718 MA10 challenge experiments, 12–14-week-old male and female mice were used with a challenge
719 dose of 5×10^5 FFU delivered in 25-30 μ l volume under anesthesia as above. For NAb treatment
720 using prophylaxis regimen, mice were treated with 250 μ g (12.5 mg/kg body weight) of indicated
721 antibodies (CV3-1, CV3-25, CV3-1 LALA, CV3-25 LALA or CV3-25 GASDALIE) or in combination
722 (CV3-1:CV3-25; 6.25 mg/kg body weight of each) via intraperitoneal injection (i.p.) 24 h prior to
723 infection. For neutralizing mAb treatment under therapeutic regimen, mice were treated at 1, 3
724 and 4 dpi intraperitoneally with CV3-1 or 3 dpi with CV3-1 LALA (12.5 mg/kg body weight). Body
725 weight was measured and recorded daily. The starting body weight was set to 100 %. For survival
726 experiments, mice were monitored every 6-12 h starting six days after virus administration.
727 Lethargic and moribund mice or mice that had lost more than 20 % of their body weight were
728 sacrificed and considered to have succumbed to infection for Kaplan-Meier survival plots.

729

730

731 **Bioluminescence Imaging (BLI) of SARS-CoV-2 infection**

732 All standard operating procedures and protocols for IVIS imaging of SARS-CoV-2 infected
733 animals under ABSL-3 conditions were approved by IACUC, IBSCYU and YARC. All the imaging
734 was carried out using IVIS Spectrum® (PerkinElmer) in XIC-3 animal isolation chamber
735 (PerkinElmer) that provided biological isolation of anesthetized mice or individual organs during
736 the imaging procedure. All mice were anesthetized via isoflurane inhalation (3 - 5 % isoflurane,
737 oxygen flow rate of 1.5 L/min) prior and during BLI using the XGI-8 Gas Anesthesia System. Prior
738 to imaging, 100 μ L of nanoluciferase substrate, furimazine (NanoGlo™, Promega, Madison, WI)
739 diluted 1:40 in endotoxin-free PBS was retroorbitally administered to mice under anesthesia. The
740 mice were then placed into XIC-3 animal isolation chamber (PerkinElmer) pre-saturated with
741 isothermia and oxygen mix. The mice were imaged in both dorsal and ventral position at indicated
742 days post infection. The animals were then imaged again after euthanasia and necropsy by
743 spreading additional 200 μ L of substrate on to exposed intact organs. Infected areas of interest
744 identified by carrying out whole-body imaging after necropsy were isolated, washed in PBS to
745 remove residual blood and placed onto a clear plastic plate. Additional droplets of furimazine in
746 PBS (1:40) were added to organs and soaked in substrate for 1-2 min before BLI.

747 Images were acquired and analyzed with the manufacturer's Living Image v4.7.3 *in vivo*
748 software package. Image acquisition exposures were set to auto, with imaging parameter

749 preferences set in order of exposure time, binning, and f/stop, respectively. Images were acquired
750 with luminescent f/stop of 2, photographic f/stop of 8. Binning was set to medium. Comparative
751 images were compiled and batch-processed using the image browser with collective luminescent
752 scales. Photon flux was measured as luminescent radiance (p/sec/cm²/sr). During luminescent
753 threshold selection for image display, luminescent signals were regarded as background when
754 minimum threshold levels resulted in displayed radiance above non-tissue-containing or known
755 uninfected regions. To determine the pattern of virus spread, the image sequences were acquired
756 every day following administration of SARS-CoV-2 (i.n). Image sequences were assembled and
757 converted to videos using Image J.

758

759 **Biodistribution of therapeutic neutralizing antibodies using IVIS**

760 Mice were intraperitoneally (i.p) administered with 250 µg of unconjugated (12.5 mg/kg body
761 weight), Alexa Fluor 647 or Alexa Fluor 594-labeled antibodies to non-infected or SARS-CoV-2
762 infected hACE2 mice. 24 h later all organs (nose, trachea, lung, cervical lymph nodes, brain, liver,
763 spleen, kidney, gut, testis and seminal vesicles) were isolated after necropsy and images were
764 acquired with an IVIS Spectrum® (PerkinElmer) and fluorescence radiance intensities were
765 analyzed with the manufacturer's Living Image v4.7.3 *in vivo* software package. Organs were cut
766 into half and weighed. One half was fixed in 4 % PFA and processed for cryoimmunohistology.
767 The other half was resuspended in serum-free RPMI and homogenized in a bead beater for
768 determination of antibody levels using quantitative ELISA.

769

770 **Measurement of therapeutic antibody levels in organs by quantitative ELISA**

771 Recombinant SARS-CoV-2 RBD and S-6P proteins were used to quantify CV3-1 and CV3-25
772 antibody levels, respectively, in mice organs. SARS-CoV-2 proteins (2.5 µg/ml), or bovine serum
773 albumin (BSA) (2.5 µg/ml) as a negative control, were prepared in PBS and were adsorbed to
774 plates (MaxiSorp; Nunc) overnight at 4 °C. Coated wells were subsequently blocked with blocking
775 buffer (Tris-buffered saline [TBS], 0.1% Tween20, 2% BSA) for 1 hour at room temperature. Wells
776 were then washed four times with washing buffer (TBS 0.1% Tween20). Titrated concentrations
777 of CV3-1 or CV3-25 or serial dilutions of mice organ homogenates were prepared in a diluted
778 solution of blocking buffer (0.1 % BSA) and incubated in wells for 90 minutes at room temperature.
779 Plates were washed four times with washing buffer followed by incubation with HRP-conjugated
780 anti-IgG secondary Abs (Invitrogen) (diluted in a diluted solution of blocking buffer [0.4% BSA])
781 for 1 hour at room temperature, followed by four washes. HRP enzyme activity was determined
782 after the addition of a 1:1 mix of Western Lightning oxidizing and luminol reagents (Perkin Elmer

783 Life Sciences). Light emission was measured with a LB941 TriStar luminometer (Berthold
784 Technologies). Signal obtained with BSA was subtracted for each organ. Titrated concentrations
785 of CV3-1 or CV3-25 were used to establish a standard curve of known antibody concentrations
786 and the linear portion of the curve was used to infer the antibody concentration in tested organ
787 homogenates.

788

789 **Cryo-immunohistology of organs**

790 Organs were isolated after necropsy and fixed in 1X PBS containing freshly prepared 4% PFA for
791 12 h at 4 °C. They were then washed with PBS, cryoprotected with 10, 20 and 30% ascending
792 sucrose series, snap-frozen in Tissue-Tek® O.C.T.™ compound and stored at -80 °C. The nasal
793 cavity was snap-frozen in 8% gelatin prepared in 1X PBS and stored at -80 °C. 10 - 30 µm thick
794 frozen sections were permeabilized with 0.2% Triton X-100 and treated with Fc receptor blocker
795 (Innovex Biosciences) before staining with indicated conjugated primary, secondary antibodies or
796 Phalloidin in PBS containing 2% BSA containing 10% fetal bovine serum. Stained sections were
797 treated with TrueVIEW Autofluorescence Quenching Kit (Vector Laboratories) and mounted in
798 VECTASHIELD® Vibrance™ Antifade Mounting Medium. Images were acquired using Nikon W1
799 spinning disk confocal microscope equipped with 405, 488, 561 and 647 nm laser lines or EVOS
800 M7000 imaging system. The images were processed using Nikon Elements AR version 4.5
801 software (Nikon Instruments Inc, Americas) and figures assembled with Photoshop CC and
802 Illustrator CC (Adobe Systems, San Jose, CA, USA).

803

804 **Focus forming assay**

805 Titers of virus stocks was determined by standard plaque assay. Briefly, the 4×10^5 Vero-E6 cells
806 were seeded on 12-well plate. 24 h later, the cells were infected with 200 µL of serially diluted
807 virus stock. After 1 hour, the cells were overlaid with 1ml of pre-warmed 0.6% Avicel (RC-581
808 FMC BioPolymer) made in complete RPMI medium. Plaques were resolved at 48 h post infection
809 by fixing in 10 % paraformaldehyde for 15 min followed by staining for 1 hour with 0.2 % crystal
810 violet made in 20 % ethanol. Plates were rinsed in water to visualize plaques.

811

812 **Measurement of viral burden**

813 Indicated organs (nasal cavity, brain, lungs from infected or uninfected mice were collected,
814 weighed, and homogenized in 1 mL of serum free RPMI media containing penicillin-streptomycin
815 and homogenized in 2 mL tube containing 1.5 mm Zirconium beads with BeadBug 6 homogenizer
816 (Benchmark Scientific, TEquipment Inc). Virus titers were measured using three highly correlative

817 methods. First, the total RNA was extracted from homogenized tissues using RNeasy plus Mini
818 kit (Qiagen Cat # 74136), reverse transcribed with iScript advanced cDNA kit (Bio-Rad Cat
819 #1725036) followed by a SYBR Green Real-time PCR assay for determining copies of SARS-
820 CoV-2 N gene RNA using primers SARS-CoV-2 N F: 5'-ATGCTGCAATCGTGCTACAA-3' and
821 SARS-CoV-2 N R: 5'-GACTGCCGCCTCTGCTC-3'.

822 Second, serially diluted clarified tissue homogenates were used to infect Vero-E6 cell culture
823 monolayer. The titers per gram of tissue were quantified using standard plaque forming assay
824 described above. Third, we used nanoluciferase activity as a shorter surrogate for plaque assay.
825 Infected cells were washed with PBS and then lysed using 1X Passive lysis buffer. The lysates
826 transferred into a 96-well solid white plate (Costar Inc) and nanoluciferase activity was measured
827 using Tristar multiwell Luminometer (Berthold Technology, Bad Wildbad, Germany) for 2.5
828 seconds by adding 20 μ l of Nano-Glo® substrate in nanoluc assay buffer (Promega Inc, WI, USA).
829 Uninfected monolayer of Vero cells treated identically served as controls to determine basal
830 luciferase activity to obtain normalized relative light units. The data were processed and plotted
831 using GraphPad Prism 8 v8.4.3.

832

833 **Analyses of signature inflammatory cytokines mRNA**

834 Brain and lung samples were collected from mice at the time of necropsy. Approximately, 20 mg
835 of tissue was suspended in 500 μ L of RLT lysis buffer, and RNA was extracted using RNeasy
836 plus Mini kit (Qiagen Cat # 74136), reverse transcribed with iScript advanced cDNA kit (Bio-Rad
837 Cat #1725036). To determine levels of signature inflammatory cytokines, multiplex qPCR was
838 conducted using iQ Multiplex Powermix (Bio Rad Cat # 1725848) and PrimePCR Probe Assay
839 mouse primers FAM-GAPDH, HEX-IL6, TEX615-CCL2, Cy5-CXCL10, and Cy5.5-IFN γ .
840 The reaction plate was analyzed using CFX96 touch real time PCR detection system. Scan mode
841 was set to all channels. The PCR conditions were 95 °C 2 min, 40 cycles of 95 °C for 10 s and
842 60 °C for 45 s, followed by a melting curve analysis to ensure that each primer pair resulted in
843 amplification of a single PCR product. mRNA levels of *Ilf6*, *Ccl2*, *Cxcl10* and *Ifng* in the cDNA
844 samples of infected mice were normalized to *Gapdh* mRNA with the formula $\Delta C_t(\text{target gene}) = C_t(\text{target gene}) - C_t(\text{Gapdh})$. The fold increase was determined using $2^{-\Delta\Delta C_t}$ method
845 comparing treated mice to uninfected controls.
846

847

848 **Antibody depletion of immune cell subsets**

849 For evaluating the effect of NK cell depletion during CV3-1 prophylaxis, anti-NK1.1 (clone PK136;
850 12.5 mg/kg body weight) or an isotype control mAb (BioXCell; clone C1.18.4; 12.5 mg/kg body

851 weight) was administered to mice by i.p. injections every 2 days starting at 48 h before SARS-
852 CoV-2-nLuc challenge till 8 dpi. The mice were bled after two days of antibody depletion, necropsy
853 or at 10 dpi (surviving mice) for analyses. To evaluate the effect of NK cell and neutrophil depletion
854 during CV3-1 therapy, anti-NK1.1 (clone PK136; 12.5 mg/kg body weight) or anti-Ly6G (clone:
855 1A8; 12.5 mg/kg body weight) was administered to mice by i.p injection every two days starting
856 at 1 dpi respectively. Rat IgG2a mAb (BioXCell; clone C1.18.4; 12.5 mg/kg body weight) was
857 used as isotype control. The mice were sacrificed and bled at 10 dpi for analyses. For evaluating
858 the effect of monocyte depletion on CV3-1 therapy, anti-CCR2 (clone MC-21; 2.5 mg/kg body
859 weight) (Mack et al., 2001) or an isotype control mAb (BioXCell; clone LTF-2; 2.5 mg/kg body
860 weight) was administered to mice by i.p injection every two days starting at 1 dpi. The mice were
861 sacrificed and bled 2-3 days after antibody administration or at 10 dpi to ascertain depletion of
862 desired population.

863

864 **Flow Cytometric Analyses**

865 For analysis of immune cell depletion, peripheral blood was collected before infection and on day
866 of harvest. Erythrocytes were lysed with RBC lysis buffer (BioLegend Inc), PBMCs fixed with 4 %
867 PFA and quenched with PBS containing 0.1M glycine. PFA-fixed cells PBMCs were resuspended
868 and blocked in Cell Staining buffer (BioLegend Inc.) containing Fc blocking antibody against
869 CD16/CD32 (BioLegend Inc) before staining with antibodies. NK cells were identified as CD3-
870 NK1.1+ cells using PE/Cy7 anti-mouse CD3(17A2) and APC anti-mouse NK-1.1 (PK136).
871 Neutrophils were identified as CD45⁺CD11b⁺Ly6G⁺ cells using APC Rat anti-mouse CD45 (30-
872 F11), PE anti-mouse CD11b (M1/70) APC/Cy7 and anti-mouse Ly-6G (1A8). Ly6C^{hi} monocytes
873 were identified as CD45⁺CD11b⁺Ly6C^{hi} cells using APC Rat anti-mouse CD45 (30-F11), PE anti-
874 mouse CD11b (M1/70) and APC/Cy7 anti-mouse Ly-6C (HK1.4). Data were acquired on an Accuri
875 C6 (BD Biosciences) and were analyzed with Accuri C6 software. FlowJo software (Treestar) was
876 used to generate FACS plot shown in Figure S7. 100,000 – 200,000 viable cells were acquired
877 for each sample.

878

879 **Sample Preparation for Electron Microscopy**

880 Lung, brain and testis tissue samples from hACE2 transgenic mice challenged intranasally with
881 SARS-CoV-2-nLuc (1 x 10⁵ FFU; 6 dpi) were imaged after necropsy using bioluminescence
882 imaging (IVIS, Perkin Elmer), pruned to isolate regions with high nLuc activity and immediately
883 pre-fixed with 3 % glutaraldehyde, 1 % paraformaldehyde, 5 % sucrose in 0.1 M sodium
884 cacodylate trihydrate to render them safe for handling outside of BSL3 containment. Viral

885 infections of cultured cells were conducted at the UVM BSL-3 facility using an approved
886 Institutional Biosafety protocol. SARS-CoV-2 strain 2019-nCoV/USA_USA-WA1/2020 (WA1;
887 generously provided by K. Plante, World Reference Center for Emerging Viruses and
888 Arboviruses, University of Texas Medical Branch) and propagated in African green monkey kidney
889 (Vero E6) cells. Vero E6 cells were maintained in complete Dulbecco's Modified Eagle Medium
890 (DMEM; Thermo Fisher, Cat. #11965–092) containing 10% fetal bovine serum (Gibco, Thermo-
891 Fisher, Cat. #16140–071), 1% HEPES Buffer Solution (15630–130), and 1% penicillin–
892 streptomycin (Thermo Fisher, Cat. #15140–122). Cells were grown in a humidified incubator at
893 37 °C with 5 % CO₂. Vero E6 cells were seeded into six well dishes and infected with SARS-CoV-
894 2 at a multiplicity of infection of 0.01 for 48 hours before fixing and preparing for electron
895 microscopy. Cells were pre-fixed with 3% glutaraldehyde, 1% paraformaldehyde, 5 % sucrose in
896 0.1M sodium cacodylate trihydrate, removed from the plates and further prepared by high-
897 pressure freezing and freeze-substitution as described below.

898 Tissues samples were further cut to ~0.5 mm³ blocks and cultured cells were gently pelleted.
899 Both samples were rinsed with fresh cacodylate buffer and placed into brass planchettes (Type
900 A; Ted Pella, Inc., Redding, CA) prefilled with 10% Ficoll in cacodylate buffer. The tissues were
901 covered with the flat side of a Type-B brass planchette and rapidly frozen with an HPM-010 high-
902 pressure freezing machine (Leica Microsystems, Vienna Austria). The frozen samples were
903 transferred under liquid nitrogen to cryotubes (Nunc) containing a frozen solution of 2.5% osmium
904 tetroxide, 0.05 % uranyl acetate in acetone. Tubes were loaded into an AFS-2 freeze-substitution
905 machine (Leica Microsystems) and processed at -90°C for 72 h, warmed over 12 h to -20°C, held
906 at that temperature for 6 h, then warmed to 4°C for 2 h. The fixative was removed, and the
907 samples rinsed 4 x with cold acetone, following which they were infiltrated with Epon-Araldite
908 resin (Electron Microscopy Sciences, Port Washington PA) over 48 h. The spleen tissue was flat-
909 embedded between two Teflon-coated glass microscope slides. Resin was polymerized at 60°C
910 for 48 h.

911

912 **Electron Microscopy and Dual-Axis Tomography**

913 Flat-embedded tissue samples or portions of cell pellets were observed with a stereo dissecting
914 microscope and appropriate regions were extracted with a microsurgical scalpel and glued to the
915 tips of plastic sectioning stubs. Semi-thin (150-200 nm) serial sections were cut with a UC6
916 ultramicrotome (Leica Microsystems) using a diamond knife (Diatome, Ltd. Switzerland). Sections
917 were placed on formvar-coated copper-rhodium slot grids (Electron Microscopy Sciences) and
918 stained with 3 % uranyl acetate and lead citrate. Gold beads (10 nm) were placed on both surfaces

919 of the grid to serve as fiducial markers for subsequent image alignment. Sections were placed in
920 a dual-axis tomography holder (Model 2040, E.A. Fischione Instruments, Export PA) and imaged
921 with a Tecnai T12-G2 transmission electron microscope operating at 120 KeV (ThermoFisher
922 Scientific) equipped with a 2k x 2k CCD camera (XP1000; Gatan, Inc. Pleasanton CA).
923 Tomographic tilt-series and large-area montaged overviews were acquired automatically using
924 the SerialEM software package (Mastronarde, 2005, 2008; Mastronarde and Held, 2017). For
925 tomography, samples were tilted +/- 62° and images collected at 1° intervals. The grid was then
926 rotated 90° and a similar series taken about the orthogonal axis. Tomographic data was
927 calculated, analyzed, and modeled using the IMOD software package (Mastronarde, 2005, 2008;
928 Mastronarde and Held, 2017) on iMac Pro and MacPro computers (Apple, Inc., Cupertino, CA).
929 Montaged projection overviews were used to illustrate spatial perspective, identify cell types and
930 frequency within the tissue sections. High-resolution 3D electron tomography was used to confirm
931 virus particles and characterize virus-containing compartments within infected cells.

932

933 **Identification and Characterization of SARS-CoV-2 Virions in infected cells and tissues.**

934 Particles resembling virions were examined in 3D by tomography to determine their identity.
935 Presumptive SARS-CoV-2 virions were identified from tomographic reconstructions of tissue
936 samples by observing structures resembling virions described in cryo-electron tomography
937 studies of purified SARS-CoV-2 and of SARS-CoV-2 in infected cells (Ke et al., 2020; Klein et al.,
938 2020; Turonova et al., 2020; Yao et al., 2020). These were compared to identified virions within
939 SARS-CoV-2–infected cultured Vero E6 cells that had been prepared for EM by the same
940 methodology (Figure 2O-Q). We used the following criteria to positively identify SARS-CoV-2
941 virions in tissues: (i) Structures that were spherical in 3D with ~60-120 nM diameters and were
942 not continuous with other adjacent structures, (ii) Spherical structures with densities
943 corresponding to a distinct membrane bilayer, internal puncta consistent with ribonucleoproteins
944 (Yao et al., 2020), and densities corresponding to surface spikes on the external peripheries of
945 the spheres. In further characterization of virions, we noted that the inner vesicles of multivesicular
946 bodies (MVBs) have been mis-identified as SARS-CoV-2 by electron microscopy (Calomeni et
947 al., 2020). We therefore compared measurements of MVB inner vesicles and presumptive
948 coronavirus virions from what we identified as intracellular exit compartments within the same
949 tomogram (data not shown) with our previous tomographic reconstructions of MVBs (He et al.,
950 2008; Ladinsky et al., 2012). We distinguished virions inside of cytoplasmic exit compartments
951 from the inner vesicles of MVBs based on differences in size (MVB inner virions are generally

952 smaller in diameter than coronaviruses) and the presence of surface spikes and internal puncta
953 (MVB inner vesicles do not present surface spikes or internal puncta).

954 **Immunoelectron microscopy.**

955 SARS-CoV-2 infected tissues were extracted and immediately fixed with 4% paraformaldehyde,
956 5% sucrose in 0.1M cacodylate buffer. Tissues were cut into ~0.5 mm³ pieces and infiltrated into
957 2.1M sucrose in 0.1M cacodylate buffer for 24 h. Individual tissue pieces were placed onto
958 aluminum cryosectioning stubs (Ted Pella, Inc.) and rapidly frozen in liquid nitrogen. Thin (100
959 nm) cryosections were cut with a UC6/FC6 cryoultramicrotome (Leica Microsystems) using a
960 cryo-diamond knife (Diatome, Ltd., Switzerland) at -110°C. Sections were picked up with a wire
961 loop in a drop of 2.3M sucrose in 0.1M cacodylate buffer and transferred to Formvar-coated,
962 carbon-coated, glow-discharged 100-mesh copper/rhodium grids (Electron Microscopy
963 Sciences). Grids were incubated 1 hr with 10% calf serum in PBS to block nonspecific antibody
964 binding, then incubated 2 hrs with anti-S antiserum (Cohen et al., 2021). Mosaic nanoparticles
965 elicit cross-reactive immune responses to zoonotic coronaviruses in mice (Cohen et al., 2021).
966 diluted 1:500 in PBS with 5% calf serum. Grids were rinsed (4x 10') with PBS then labeled for 2
967 hrs with 10 nm gold conjugated goat anti-mouse secondary antibody (Ted Pella, Inc.). Grids were
968 again rinsed (4x 10') with PBS, then 3x with distilled water and negatively stained with 1% uranyl
969 acetate in 1% methylcellulose (Sigma) for 20'. Grids were air-dried in wire loops and imaged as
970 described for ET.

971

972 **Protein expression and purification**

973 FreeStyle 293F cells (Thermo Fisher Scientific) were grown in FreeStyle 293F medium (Thermo
974 Fisher Scientific) to a density of 1x10⁶ cells/mL at 37°C with 8% CO₂ with regular agitation (150
975 rpm). Cells were transfected with a plasmid coding for recombinant stabilized SARS-CoV-2
976 ectodomain (S-6P; obtained from Dr. Jason S. McLellan) or SARS-CoV-2 RBD (Beaudoin-
977 Bussieres et al., 2020) using ExpiFectamine 293 transfection reagent, as directed by the
978 manufacturer (Thermo Fisher Scientific). One-week post-transfection, supernatants were clarified
979 and filtered using a 0.22 µm filter (Thermo Fisher Scientific). The recombinant S-6P was purified
980 by strep-tactin resin (IBA) following by size-exclusion chromatography on Superose 6 10/300
981 column (GE Healthcare) in 10 mM Tris pH 8.0 and 200 mM NaCl (SEC buffer). RBD was purified
982 by Ni-NTA column (Invitrogen) and gel filtration on Hiload 16/600 Superdex 200pg using the same
983 SEC buffer. Purified proteins were snap-frozen at liquid nitrogen and stored in aliquots at 80°C
984 until further use. Protein purities were confirmed as one single-band on SDS-PAGE.

985

986 **SARS-CoV-2 Spike ELISA (enzyme-linked immunosorbent assay)**

987 The SARS-CoV-2 Spike ELISA assay used was recently described (Beaudoin-Bussieres et al.,
988 2020; Prevost et al., 2020). Briefly, recombinant SARS-CoV-2 S-6P and RBD proteins (2.5 µg/ml),
989 or bovine serum albumin (BSA) (2.5 µg/ml) as a negative control, were prepared in PBS and were
990 adsorbed to plates (MaxiSorp; Nunc) overnight at 4 °C. Coated wells were subsequently blocked
991 with blocking buffer (Tris-buffered saline [TBS] containing 0.1% Tween20 and 2% BSA) for 1 hour
992 at room temperature. Wells were then washed four times with washing buffer (TBS containing
993 0.1% Tween20). CV3-1, CV3-25 and CR3022 mAbs (50 ng/ml) were prepared in a diluted solution
994 of blocking buffer (0.1 % BSA) and incubated with the RBD-coated wells for 90 minutes at room
995 temperature. Plates were washed four times with washing buffer followed by incubation with HRP-
996 conjugated anti-IgG secondary Abs (Invitrogen) (diluted in a diluted solution of blocking buffer
997 [0.4% BSA]) for 1 hour at room temperature, followed by four washes. HRP enzyme activity was
998 determined after the addition of a 1:1 mix of Western Lightning oxidizing and luminol reagents
999 (Perkin Elmer Life Sciences). Light emission was measured with a LB941 TriStar luminometer
1000 (Berthold Technologies). Signal obtained with BSA was subtracted for each plasma and was then
1001 normalized to the signal obtained with CR3022 mAb present in each plate.

1002

1003 **Flow cytometry analysis of cell-surface Spike staining.**

1004 Spike expressors of human coronaviruses SARS-CoV-2, SARS-CoV-1, MERS-CoV, OC43, NL63
1005 and 229E were reported elsewhere (Hoffmann et al., 2020; Hoffmann et al., 2013; Hofmann et
1006 al., 2005; Park et al., 2016; Prevost et al., 2020). Expressors of HKU1 Spike and SARS-CoV-2
1007 S2 N-His were purchased from Sino Biological. Using the standard calcium phosphate method,
1008 10 µg of Spike expressor and 2 µg of a green fluorescent protein (GFP) expressor (pIRES2-
1009 eGFP) was transfected into 2×10^6 293T cells. At 48 hours post transfection, 293T cells were
1010 stained with CV3-1 and CV3-25 antibodies (5µg/mL), using cross-reactive anti-SARS-CoV-1
1011 Spike CR3022 or mouse anti-His tag (Sigma-Aldrich) as positive controls. Alexa Fluor-647-
1012 conjugated goat anti-human IgG (H+L) Abs (Invitrogen) and goat anti-mouse IgG (H+L) Abs
1013 (Invitrogen) were used as secondary antibodies. The percentage of transfected cells (GFP+ cells)
1014 was determined by gating the living cell population based on the basis of viability dye staining
1015 (Aqua Vivid, Invitrogen). Samples were acquired on a LSRII cytometer (BD Biosciences) and data
1016 analysis was performed using FlowJo v10 (Tree Star).

1017

1018 **Virus capture assay**

1019 The SARS-CoV-2 virus capture assay was previously reported (Ding et al., 2020). Briefly,
1020 pseudoviral particles were produced by transfecting 2×10^6 HEK293T cells with pNL4.3 Luc R-E-
1021 (3.5 μ g), plasmids encoding for SARS-CoV-2 Spike or SARS-CoV-1 Spike (3.5 μ g) protein and
1022 VSV-G (pSVCMV-IN-VSV-G, 1 μ g) using the standard calcium phosphate method. Forty-eight
1023 hours later, supernatant-containing virion was collected, and cell debris was removed through
1024 centrifugation (1,500 rpm for 10 min). To immobilize antibodies on ELISA plates, white MaxiSorp
1025 ELISA plates (Thermo Fisher Scientific) were incubated with 5 μ g/ml of antibodies in 100 μ l
1026 phosphate-buffered saline (PBS) overnight at 4°C. Unbound antibodies were removed by
1027 washing the plates twice with PBS. Plates were subsequently blocked with 3% bovine serum
1028 albumin (BSA) in PBS for 1 hour at room temperature. After two washes with PBS, 200 μ l of virus-
1029 containing supernatant was added to the wells. After 4 to 6 hours incubation, supernatants were
1030 removed and the wells were washed with PBS 3 times. Virus capture by any given antibody was
1031 visualized by adding 1×10^4 SARS-CoV-2-resistant Cf2Th cells per well in complete DMEM
1032 medium. Forty-eight hours post-infection, cells were lysed by the addition of 30 μ L of passive lysis
1033 buffer (Promega) and three freeze-thaw cycles. An LB941 TriStar luminometer (Berthold
1034 Technologies) was used to measure the luciferase activity of each well after the addition of 100
1035 μ L of luciferin buffer (15 mM MgSO₄, 15 mM KH₂PO₄ [pH 7.8], 1 mM ATP, and 1 mM dithiothreitol)
1036 and 50 μ L of 1 mM D-luciferin potassium salt (ThermoFisher Scientific).

1037

1038 **Surface plasmon resonance (SPR)**

1039 All surface plasma resonance assays were performed on a Biacore 3000 (GE Healthcare) with a
1040 running buffer of 10 mM HEPES pH 7.5 and 150 mM NaCl, supplemented with 0.05% Tween 20
1041 at 25°C. The binding affinity and kinetics to the SARS-CoV-2 spike (S) trimer (SARS-CoV-2 S
1042 HexaPro [S-6P]) (Hsieh et al., 2020) and SARS-CoV-2 S2 ectodomain (baculovirus produced his-
1043 tagged S2(686-1213) from BEI Resources (NR-53799) were evaluated using monovalent CV3-1
1044 and CV3-25 Fab. Fabs were generated by standard papain digestion (Thermo Fisher) and purified
1045 by Protein A affinity chromatography and gel filtration. His-tagged SARS-CoV-2 S-6P or SARS-
1046 CoV-2 S2 ectodomain was immobilized onto a Ni-NTA sensor chip at a level of ~1000 and ~630
1047 RU response units (RUs), respectively. Two-fold serial dilutions of CV3-1 or CV3-25 Fab were
1048 injected in a concentration range of 1.56-100 nM over the SARS-CoV-2 S-6P and CV3-25 Fab in
1049 a range of 3.125 to 200 nM over the SARS-CoV-2 S2. After each cycle the Ni-NTA sensor chip
1050 was regenerated with a wash step of 0.1 M EDTA and reloaded with 0.1 M nickel sulfate followed
1051 by the immobilization of fresh antigens for the next cycle. The binding kinetics of SARS-CoV-2
1052 RBD and CV3-1 were obtained in a format where CV3-1 IgG was immobilized onto a Protein A

1053 sensor chip (Cytiva) with ~300 (RUs) and serial dilutions of SARS-CoV-2 RBD were injected with
1054 concentrations ranging from 1.56 to 50 nM. The protein A chip was regenerated with a wash step
1055 of 0.1 M glycine pH 2.0 and reloaded with IgG after each cycle.

1056 All sensograms were corrected by subtraction of the corresponding blank channel and the kinetic
1057 constant determined using a 1:1 Langmuir model with the BIA evaluation software (GE
1058 Healthcare). Goodness of fit of the curve was evaluated by the Chi² value with a value below 3
1059 considered acceptable

1060

1061 **Pseudovirus neutralization assay**

1062 Target cells were infected with single-round luciferase-expressing lentiviral particles. Briefly, 293T
1063 cells were transfected by the calcium phosphate method with the pNL4.3 R-E- Luc plasmid (NIH
1064 AIDS Reagent Program) and a plasmid encoding for SARS-CoV-2 Spike at a ratio of 5:4. Two
1065 days post-transfection, cell supernatants were harvested and stored at -80°C until use. 293T-
1066 ACE2 (Prevost et al., 2020) target cells were seeded at a density of 1×10^4 cells/well in 96-well
1067 luminometer-compatible tissue culture plates (Perkin Elmer) 24 h before infection. Recombinant
1068 viruses in a final volume of 100 μ L were incubated with the indicated semi-log diluted antibody
1069 concentrations for 1 h at 37°C and were then added to the target cells followed by incubation for
1070 48 h at 37°C; cells were lysed by the addition of 30 μ L of passive lysis buffer (Promega) followed
1071 by one freeze-thaw cycle. An LB941 TriStar luminometer (Berthold Technologies) was used to
1072 measure the luciferase activity of each well after the addition of 100 μ L of luciferin buffer (15 mM
1073 MgSO₄, 15 mM KH₂PO₄ [pH 7.8], 1 mM ATP, and 1 mM dithiothreitol) and 50 μ L of 1 mM d-
1074 luciferin potassium salt. The neutralization half-maximal inhibitory dilution (IC₅₀) represents the
1075 plasma dilution to inhibit 50 % of the infection of 293T-ACE2 cells by recombinant viruses bearing
1076 the SARS-CoV-2 S glycoproteins.

1077

1078 **Microneutralization assay**

1079 A microneutralization assay for SARS-CoV-2 serology was performed as previously described
1080 (Amanat et al., 2020). Experiments were conducted with the SARS-CoV-2 USA-WA1/2020 virus
1081 strain (obtained from BEI resources). One day prior to infection, 2×10^4 Vero E6 cells were seeded
1082 per well of a 96 well flat bottom plate and incubated overnight at 37°C under 5% CO₂ to permit
1083 cell adherence. Titrated antibody concentrations were performed in a separate 96 well culture
1084 plate using MEM supplemented with penicillin (100 U/mL), streptomycin (100 mg/mL), HEPES,
1085 L-Glutamine (0.3 mg/mL), 0.12% sodium bicarbonate, 2% FBS (all from Thermo Fisher Scientific)
1086 and 0.24% BSA (EMD Millipore Corporation). In a Biosafety Level 3 laboratory (ImPaKT Facility,

1087 Western University), 10^3 TCID₅₀/mL of SARS-CoV-2 USA-WA1/2020 live virus was prepared in
1088 MEM + 2% FBS and combined with an equivalent volume of respective antibody dilutions for one
1089 hour at room temperature. After this incubation, all media was removed from the 96 well plate
1090 seeded with Vero E6 cells and virus:antibody mixtures were added to each respective well at a
1091 volume corresponding to 600 TCID₅₀ per well and incubated for one hour further at 37°C. Both
1092 virus only and media only (MEM + 2% FBS) conditions were included in this assay. All
1093 virus:plasma supernatants were removed from wells without disrupting the Vero E6 monolayer.
1094 Each antibody concentration (100 µL) was added to its respective Vero E6-seeded well in addition
1095 to an equivalent volume of MEM + 2% FBS and was then incubated for 48 hours. Media was then
1096 discarded and replaced with 10% formaldehyde for 24 hours to cross-link Vero E6 monolayer.
1097 Formaldehyde was removed from wells and subsequently washed with PBS. Cell monolayers
1098 were permeabilized for 15 minutes at room temperature with PBS + 0.1% Triton X-100, washed
1099 with PBS and then incubated for one hour at room temperature with PBS + 3% non-fat milk. An
1100 anti-mouse SARS-CoV-2 nucleocapsid protein (Clone 1C7, Bioss Antibodies) primary antibody
1101 solution was prepared at 1 mg/mL in PBS + 1% non-fat milk and added to all wells for one hour
1102 at room temperature. Following extensive washing with PBS, an anti-mouse IgG HRP secondary
1103 antibody solution was formulated in PBS + 1% non-fat milk. One-hour post-incubation, wells were
1104 washed with PBS, SIGMAFAST OPD developing solution (Millipore Sigma) was prepared as per
1105 manufacturer's instructions and added to each well for 12 minutes. Dilute HCl (3.0 M) was added
1106 to quench the reaction and the optical density at 490 nm of the culture plates was immediately
1107 measured using a Synergy LX multi-mode reader and Gen5 microplate reader and imager
1108 software (BioTek).

1109

1110 **SARS-CoV-2 MA10 neutralization assay**

1111 Serial two-fold dilutions of CV3-1 antibody (100 to 0.0078125 mg/mL) were prepared in triplicates
1112 in a volume of 50 µL. 30 µL of MA10 virus (1.2×10^4 FFU/mL stock) was mixed with diluted
1113 antibody and incubated for 1 h at 37°C. The virus-antibody mixes were then added to Vero E6
1114 cells (7.5×10^5 cells/well) seeded 24 h earlier, in 6-well tissue culture plates and allowed to interact
1115 with cells for 1 h. The cells were then overlaid with 1 mL of pre-warmed 0.6 % Avicel (RC-581
1116 FMC BioPolymer) made in complete RPMI medium. Plaques were resolved after 48 h by fixing
1117 cells in 10 % paraformaldehyde for 15 min followed by staining for 1 hour with 0.2 % crystal violet
1118 made in 20 % ethanol. Plates were rinsed in water to visualize FFU. The FFU counts from virus
1119 samples without antibody incubation were set to 100% (50 - 60 FFU/well). IC₅₀ was calculated by

1120 plotting the log (antibody dilution) vs normalized FFUs and using non-linear fit option in GraphPad
1121 Prism.

1122

1123 **Cell-to-cell fusion assay**

1124 To assess cell-to-cell fusion, 2×10^6 293T cells were co-transfected with plasmid expressing HIV-
1125 1 Tat (1 μ g) and a plasmid expressing SARS-CoV-2 Spike (4 μ g) using the calcium phosphate
1126 method. Two days after transfection, Spike-expressing 293T (effector cells) were detached with
1127 PBS-EDTA 1mM and incubated for 1 hour with indicated amounts of CV3-1 and/or CV3-25 NAb
1128 at 37°C and 5% CO₂. Subsequently, effector cells (1×10^4) were added to TZM-bl-ACE2 target
1129 cells that were seeded at a density of 1×10^4 cells/well in 96-well luminometer-compatible tissue
1130 culture plates 24 h before the assay. Cells were co-incubated for 6 h at 37°C and 5% CO₂, after
1131 which they were lysed by the addition of 40 μ L of passive lysis buffer (Promega) and one freeze-
1132 thaw cycles. An LB 941 TriStar luminometer (Berthold Technologies) was used to measure the
1133 luciferase activity of each well after the addition of 100 μ L of luciferin buffer (15 mM MgSO₄, 15
1134 mM KH₂PO₄ [pH 7.8], 1 mM ATP, and 1 mM dithiothreitol) and 50 μ L of 1 mM d-luciferin potassium
1135 salt (ThermoFisher Scientific).

1136

1137 **Antibody dependent cellular cytotoxicity (ADCC) assay**

1138 For evaluation of anti-SARS-CoV-2 ADCC activity, parental CEM.NKr CCR5+ cells were mixed
1139 at a 1:1 ratio with CEM.NKr-Spike cells. These cells were stained for viability (AquaVivid; Thermo
1140 Fisher Scientific) and a cellular dye (cell proliferation dye eFluor670; Thermo Fisher Scientific)
1141 and subsequently used as target cells. Overnight rested PBMCs were stained with another
1142 cellular marker (cell proliferation dye eFluor450; Thermo Fisher Scientific) and used as effector
1143 cells. Stained effector and target cells were mixed at a 10:1 ratio in 96-well V-bottom plates.
1144 Titrated concentrations of CV3-1 and CV3-25 mAbs were added to the appropriate wells. The
1145 plates were subsequently centrifuged for 1 min at 300xg, and incubated at 37°C, 5% CO₂ for 5
1146 hours before being fixed in a 2% PBS-formaldehyde solution.

1147 ADCC activity was calculated using the formula: $[(\% \text{ of GFP+ cells in Targets plus Effectors}) - (\% \text{ of GFP+ cells in Targets plus Effectors plus antibody})] / (\% \text{ of GFP+ cells in Targets}) \times 100$ by
1148 gating on transduced live target cells. All samples were acquired on an LSRII cytometer (BD
1149 Biosciences) and data analysis performed using FlowJo v10 (Tree Star).

1151

1152 **Antibody dependent cellular phagocytosis (ADCP) assay**

1153 The ADCP assay was performed using CEM.NKr-Spike cells as target cells that were
1154 fluorescently labelled with a cellular dye (cell proliferation dye eFluor450). THP-1 cells were used
1155 as effector cells and were stained with another cellular dye (cell proliferation dye eFluor670).
1156 Stained target and effector cells were mixed at a 5:1 ratio in 96-well U-bottom plates. Titrated
1157 concentrations of CV3-1 and CV3-25 mAbs were added to the appropriate wells. After an
1158 overnight incubation at 37 °C and 5% CO₂, cells were fixed with a 2% PBS-formaldehyde solution.
1159 Antibody-mediated phagocytosis was determined by flow cytometry, gating on THP-1 cells that
1160 were double-positive for efluor450 and efluor670 cellular dyes. All samples were acquired on an
1161 LSRII cytometer (BD Biosciences) and data analysis performed using FlowJo v10 (Tree Star).

1162

1163 **smFRET imaging of S on SARS-CoV-2 VLPs (S-MEN particles)**

1164 S-MEN coronavirus-like particles carrying SARS-CoV-2 spikes were prepared similarly as
1165 previously described (Lu et al., 2020). The peptides tags-carrying spike plasmid (pCMV-S Q3-1
1166 A4-1: Q3 - GQQQLG; A4 - DSLDMLEM) was used to make S-MEN coronavirus-like particles.
1167 Plasmids encoding wildtype pCMV-S, dual-tagged pCMV-S Q3-1 A4-1, pLVX-M, pLVX-E, and
1168 pLVX-N were transfected into 293T cells at a ratio of 20:1:21:21:21. Using this very diluted ratio
1169 of tagged-S vs. wildtype S, the vast majority of S-MEN particles carry wildtype spikes. For the rest
1170 of the virus particles containing tagged S, more than 95 % S trimers will have one dual-tagged
1171 protomer and two wildtype protomers within a trimer. Using this strategy, we generated S-MEN
1172 particles with an average of one dual-tagged S protomer for conjugating FRET-paired
1173 fluorophores among predominantly wildtype S trimers presented on VLP surface. S-MEN particles
1174 were harvested 40 h post-transfection, filtered with a 0.45 µm pore size filter, and partially purified
1175 using ultra-centrifugation at 25,000 rpm for 2 h through a 15 % sucrose cushion made in PBS. S-
1176 MEN particles were then re-suspended in 50 mM pH 7.5 HEPES buffer, labeled with Cy3B(3S)
1177 and Cy5 derivative (LD650-CoA) and purified through an optiprep gradient as previously
1178 described (Lu et al., 2019; Lu et al., 2020; Munro et al., 2014)

1179 smFRET images of S-MEN particles was acquired on a home-built prism-based total internal
1180 reflection fluorescence (TIRF) microscope, as described previously (Lu et al., 2020). smFRET
1181 data analysis was performed using MATLAB (MathWorks)-based customized SPARTAN software
1182 package (Juetten et al., 2016). The conformational effects of 50 µg/ml CV3-1 and CV3-25
1183 antibodies on SARS-CoV-2 spike were tested by pre-incubating fluorescently labeled viruses for
1184 60 mins at 37 °C before imaging in the continued presence of the antibodies. During smFRET
1185 imaging, fluorescently-labeled S-MEN particles were monitored for 80 seconds, where

1186 fluorescence from Cy3B(3S) and LD650-CoA labeled on S-MEN particles was recorded
1187 simultaneously at 25 frames per second for 80 seconds. Donor (Cy3B(3S)) and acceptor (LD650-
1188 CoA) fluorescence intensity traces were extracted after subtracting background signals and
1189 correcting cross-talks. The energy transfer efficiency (FRET) traces were generated from
1190 fluorescence intensity traces, according to $FRET = \frac{I_A}{\gamma I_D + I_A}$, where I_D and I_A are the fluorescence
1191 intensities of donor and acceptor, respectively, γ is the correlation coefficient compromising the
1192 discrepancy in quantum yields and detection efficiencies of two fluorophores. FRET is sensitive
1193 to changes in distances between the donor and the acceptor over time, ultimately translating into
1194 the conformational profiles and dynamics of S on S-MEN particles. S-MEN particles that contain
1195 incomplete FRET-paired fluorophores or more than one FRETing pairs of donor and acceptor on
1196 a single virus particle were automatically filtered from virus pools for further analysis. FRET traces
1197 of fluorescently-labeled S-MEN particles which meet the criteria of sufficient signal-to-noise ratio
1198 and anti-correlated fluctuations in donor and acceptor fluorescence intensity are indicative of live
1199 molecules. These FRET traces, indicated the number of traces in Figure 3, were then compiled
1200 into FRET histograms in Figure 3. Each FRET histogram was fitted into the sum of four Gaussian
1201 distributions in Matlab, where each Gaussian distribution represents one conformation and the
1202 area under each Gaussian curve estimates the occupancy.

1203

1204 **Quantification and Statistical Analysis**

1205 Data were analyzed and plotted using GraphPad Prism software (La Jolla, CA, USA). Statistical
1206 significance for pairwise comparisons were derived by applying non-parametric Mann-Whitney
1207 test (two-tailed). To obtain statistical significance for survival curves, grouped data were
1208 compared by log-rank (Mantel-Cox) test. To obtain statistical significance for grouped data we
1209 employed 2-way ANOVA followed by Dunnett's or Tukey's multiple comparison tests.

1210 p values lower than 0.05 were considered statistically significant. P values were indicated as *, p
1211 < 0.05; **, p < 0.01; ***, p < 0.001; ****, p < 0.0001.

1212

1213 **Schematics**

1214 Schematics for showing experimental design in figures and graphical abstract were created with
1215 BioRender.com.

1216

1217 **Supplementary Figure Legends:**

1218 **Figure S1. Widespread SARS-CoV-2 Infection in K18-hACE2 Mice. Related to Figure 1. (A)**

1219 Images of cryosections from indicated tissues of SARS-CoV-2-nLuc infected K18-hACE2 mouse
1220 harvested at 6 dpi. Actin (green), nucleocapsid (red) and hACE2 (magenta) were detected using
1221 phalloidin and respective antibodies. Notably, hACE2 appeared as puncta on the surface of
1222 infected neurons and lung tissue compared to other organs where the signal was more uniform
1223 and stained a region of the cell surface. Scale bar: 50 μ m

1224 (B) Images of cryosections from brain tissues of SARS-CoV-2-nLuc infected K18-hACE2 mouse
1225 harvested at 6 dpi to characterize infected cells. Glial cells (top panel) were identified using
1226 antibodies to markers CD68 (magenta) and CD11b (green). Neurons (lower panel) were identified
1227 using antibodies to MAP2 (green) and mature astrocytes were identified using antibodies to GFAP
1228 (magenta). SARS-CoV-2 infected cells were identified using antibodies to nucleocapsid (red).
1229 Nucleocapsid positive cells were predominantly positive for MAP2. Scale bar: 20 μ m

1230 (C) Images of cryosections from lung and brain tissues of SARS-CoV-2-nLuc infected K18-hACE2
1231 mouse harvested at 6 dpi to visualize neutrophil and inflammatory monocyte infiltration.
1232 Monocytes and neutrophils were identified using antibodies to markers Ly6C (magenta) and Ly6G
1233 (green) respectively. SARS-CoV-2 infected cells were identified using antibodies to nucleocapsid
1234 (red) and actin (blue) was stained using phalloidin conjugated to AF₄₀₅. Scale bar: 20 μ m

1235

1236 **Figure S2. Widespread Biodistribution of CV3-25 and CV3-1 NABs in Mice 24 h After**
1237 **Intraperitoneal Delivery. Related to Figure 3.**

1238 (A) C57BL/6J mice were either mock treated (PBS) or intraperitoneally administered 12.5
1239 mg/kg body weight of CV3-25 monoclonal antibody conjugated to Alexa Fluor 594 (CV3-25 AF₅₉₄).
1240 24 h later, indicated tissues were imaged using the fluorescence module in IVIS spectrum to
1241 detect AF₅₉₄. The plot shows the quantified radiance detected in indicated tissues after
1242 normalization with corresponding organs from control mouse.

1243 (B) Images of cryosections from indicated tissues from CV3-25 AF₅₉₄-treated mouse as in A. Actin
1244 and CV3-25 were detected using phalloidin-AF₄₈₈ and AF₆₄₇ conjugated anti-human IgG
1245 respectively. Scale bar: 20 μ m

1246 (C) C57BL/6J mice were either mock treated (PBS) or intraperitoneally administered 12.5
1247 mg/kg of CV3-1 monoclonal antibody conjugated to Alexa Fluor 647 (CV3-1 AF₆₄₇). 24 h later,
1248 indicated tissues were imaged using the fluorescence module in IVIS spectrum to detect AF₆₄₇.
1249 The plot shows the quantified radiance detected in indicated tissues after normalization with
1250 corresponding organs from control mouse.

1251 (B) Images of cryosections from indicated tissues from CV3-1 AF₆₄₇-treated mouse as in A. Actin
1252 was detected using phalloidin-AF₄₈₈. CV3-1 AF₆₄₇ was detected in the red channel using Alexa
1253 Fluor 568 conjugated anti-human IgG. Scale bar: 20 μ m

1254

1255 **Figure S3. Assessment of CV3-1 and CV3-25 NAbs Biodistribution in Mice Using ELISA**
1256 **and Immunohistology. Related to Figure 4.**

1257 (A-D) Estimation of CV3-25 and CV3-1 NAbs biodistribution in mice using ELISA. Measurement
1258 of anti-Spike NAbs levels in organs was performed using quantitative ELISA. (A-B) Recombinant
1259 SARS-CoV-2 RBD and (C-D) S-6P proteins were used to quantify CV3-1 and CV3-25 antibody
1260 levels, respectively. Linear standard curves using known concentrations of CV3-1 or CV3-25
1261 NAbs were established for inferring the antibody concentration in organ homogenates. Serial
1262 dilutions of homogenized mice organs were prepared in PBS and incubate on antigen-coated
1263 plates. The presence of anti-Spike NAbs was revealed using HRP-conjugated anti-human IgG
1264 secondary Abs. The signal obtained with BSA (negative control) was subtracted for each organ.
1265 Relative light unit (RLU) values were transformed into a NAb concentrations based on the
1266 standard curve and the dilution factor. Subsequently, these concentration values were multiplied
1267 with the homogenization volume and divided by the total organ weight.

1268 (E) Persistence and redistribution of neutralizing NABs in SARS-CoV-2 infected mice. Images of
1269 brain tissue from K18-hACE2 mice infected with SARS-CoV-2-nLuc at 6 dpi that were
1270 prophylactically treated with CV3-1 or CV3-25 (12.5 mg/kg body weight), 24 h before infection.
1271 Actin (green) was labelled using phalloidin, CV3-1 and CV3-25 (magenta) were detected using
1272 anti-hlgG conjugated to AF₆₄₇ and infected cells (red) were identified using antibodies to SARS-
1273 CoV-2 N. CV3-1 localizes to the endothelial walls of blood vessels and CV3-25 redistributes to
1274 decorate infected neurons in addition to endothelium (seen in UI mice; Figure S2). Scale bar: 50
1275 μm

1276 (F) Assessment of neutrophil infiltration in the brains of CV3-25 and CV3-1-pretreated mice for an
1277 experiment as in E. Neutrophils were identified using antibodies to marker Ly6G (magenta) and
1278 SARS-CoV-2 infected cells were identified using antibodies to nucleocapsid (red) and actin (blue)
1279 was stained using phalloidin conjugated to AF₄₀₅. Scale bar: 20 μm

1280

1281 **Figure S4. Efficacious Dose for CV3-1 NAb During Prophylaxis. Related to Figure 4.**

1282 (A) A scheme showing experimental design for testing the dose of CV3-1 NAb to achieve
1283 protection for lethal SARS-CoV-2-nLuc infection. Indicated concentration of CV3-1 NAb was
1284 delivered (i.p.) 1 day before challenging K18-hACE2 mice with 1×10^5 FFU of SARS-CoV-2 nLuc.
1285 Human IgG1-treated (12.5 mg/kg) mice were used as control (isotype treated). Mice were
1286 followed by non-invasive BLI every 2 days from the start of infection using IVIS Spectrum after
1287 retroorbital administration of furimazine (nLuc substrate).

1288 (B) SARS-CoV-2 replication and dissemination in K18-hACE2 transgenic mice (n = 4-6 per group)
1289 for experiment as in A, were monitored via BLI in ventral (v) and dorsal (d) positions at the
1290 indicated days post infection every 2 days. Images from two mice under CV3-1 prophylaxis (0.7
1291 mg/kg) are shown where one mouse succumbed at 6 dpi and the other survived despite weak but
1292 observable neuroinvasion. Images from one representative experiment are shown for the rest.

1293 (C-D) A plot showing temporal quantification of nLuc signal acquired non-invasively and displayed
1294 as photon flux (photons/sec) in whole body or brain region of SARS-CoV2-nLuc infected K18-
1295 hACE2 mice for an experiment as in A. Each curve represents luminescent signal computed for
1296 individual mouse. Scale bars denote radiance in photons per second per square centimeter per
1297 steradian (p/sec/cm²/sr).

1298 (E) A plot showing temporal body weight changes in indicated groups of K18-hACE2 mice at
1299 indicated days post infection for an experiment shown in A. Each curve represents one animal.
1300 The body weight at the start of the experiment was set to 100 %.

1301 (F) Kaplan-Meier survival curves of mice statistically compared by log-rank (Mantel-Cox) test for
1302 experiment as in A.

1303 (G) Plot showing viral loads as nLuc activity/mg of indicated organs using Vero E6 cells as targets.
1304 Undetectable virus amounts were set to 1 for display on log plots.

1305 Grouped data in (C)-(E) and G were analyzed by 2-way ANOVA followed by Dunnett's or Tukey's
1306 multiple comparison tests. Statistical significance: group comparisons to isotype control are
1307 shown in black; group comparisons to CV3-1 (0.7 mg/kg) are shown in red. *, $p < 0.05$; **, $p <$
1308 0.01 ; ***, $p < 0.001$; ****, $p < 0.0001$; Mean values \pm SD are depicted.

1309

1310 **Figure S5. LALA Mutations Diminish and GASDALIE Mutations Enhance Antibody Effector**
1311 **Functions of NABs without Compromising Neutralizing Activity. Related to Figure 6.**

1312 (A) Cell-surface staining of CEM.NKr cells stably expressing full-length SARS-CoV-2 Spike
1313 (CEM.NKr-Spike) using CV3-1 and CV3-25 mAbs or their LALA and GASDALIE mutant
1314 counterparts. The graph shown represent the mean fluorescence intensities (MFI)
1315 obtained with titrated concentrations of anti-Spike NABs. MFI values obtained with
1316 parental CEM.NKr were subtracted.

1317 (B) Pseudoviral particles encoding for the luciferase reporter gene and bearing the SARS-CoV-2
1318 S glycoproteins were used to infect 293T-ACE2 cells. Neutralizing activity was measured by
1319 incubating pseudoviruses with titrated concentrations of anti-Spike NAbS at 37°C for 1 h prior to
1320 infection of 293T-ACE2 cells. Neutralization half maximal inhibitory antibody concentration (IC₅₀)
1321 values were determined using a normalized non-linear regression using GraphPad Prism
1322 software.

1323 (C) Using a FACS-based ADCC assay, CEM.NKr parental cells were mixed at a 1:1 ratio
1324 with CEM.NKr-Spike cells and were used as target cells. PBMCs from uninfected donors were
1325 used as effector cells. The graph shown represent the percentages of ADCC obtained in the
1326 presence of titrated concentrations of anti-Spike NAbS.

1327 (D) Using a FACS-based ADCP assay, CEM.NKr-Spike cells were used as target cells and THP-
1328 1 monocytic cell line was used as effector cells. The graph shown represent the percentages
1329 of effector cells that had phagocytosed target cells obtained in the presence of titrated
1330 concentrations of anti-Spike NAbS. Statistical significance was tested using a non-parametric
1331 Mann-Whitney test for pairwise comparison between WT and LALA NAbS (*, $p < 0.05$; **, $p <$
1332 0.01 ; ns, not significant)

1333 (E-F) Biodistribution of LALA and GASDALIE mutants of indicated NAbS in mice 24 h after i.p.
1334 delivery. B6 mice were either isotype treated (control) or intraperitoneally administered of Alexa
1335 Fluor 647 conjugated NAb mutants (12.5 mg/kg body weight). 24 h later, indicated tissues were
1336 imaged using the fluorescence module in IVIS spectrum to detect Alexa Fluor 647. The plot shows
1337 the quantified radiance detected in indicated tissues after normalization with corresponding
1338 organs from control mouse.

1339 (G, H) Images of cryosections from brain tissues of K18-hACE2 mice pretreated with LALA
1340 mutants of CV3-25 or CV3-1 (i.p., 12.5 mg/g body weight) at 6 dpi. Actin was detected using
1341 phalloidin-Alexa Fluor 488. CV3-25 and CV3-1 (magenta) were detected using Alexa Fluor 647
1342 conjugated anti-human IgG respectively. Infected cells were detected using antibodies to SARS-

1343 CoV-2 nucleocapsid (red). Images show penetration of both CV3-25 and CV3-1 mAbs into the
1344 brain and localization to the surface of infected neurons. Scale bar: 20 μm

1345 (I) SARS-CoV-2 can establish infection in nasal cavity and lungs during CV3-1 prophylaxis. A
1346 scheme showing experimental design to test establishment of virus infection in K18-hACE2 mice
1347 pretreated with CV3-1 NAb (i.p., 12.5 mg/kg body weight), 1 day before challenging with 1×10^5
1348 FFU of SARS-CoV-2 nLuc. Mice treated similarly with Isotype matched hlgG1 were used as
1349 controls. The mice were followed by non-invasive BLI at 0 and 3 dpi using IVIS Spectrum after
1350 retroorbital administration of furimazine (nLuc substrate).

1351 (J) SARS-CoV-2 replication and dissemination in indicated groups of K18-hACE2 transgenic mice
1352 ($n = 5-3$ per group) for experiment as in I, were monitored via BLI at the indicated times. The mice
1353 were euthanized at 3 dpi and imaged again after necropsy. Images from one representative
1354 experiment are shown.

1355 (K) A plot showing temporal quantification of nLuc signal acquired non-invasively and displayed
1356 as photon flux (photons/sec) in whole body of SARS-CoV2-nLuc infected K18-hACE2 mice for an
1357 experiment as in I. Each line represents luminescent signal computed for individual mouse.

1358 (L, M) *Ex vivo* imaging of indicated organs after necropsy at 3 dpi and quantification of nLuc
1359 signal displayed as photon flux (photons/sec) in K18-ACE2 mice for experiment as in I.

1360 (N) A plot showing real-time PCR analyses to detect SARS-CoV-2 nucleocapsid (N) gene mRNA
1361 in indicated organs of K18-hACE2 mice for an experiment as in I. The data were normalized to N
1362 gene mRNA seen in uninfected mice and *Gapdh* mRNA levels. Scale bars denote radiance
1363 (photons/sec/cm²/steradian). *p* values obtained by non-parametric Mann-Whitney test for pairwise
1364 comparison with isotype-treated controls; *, $p < 0.05$; **, $p < 0.01$; ***, $p < 0.001$; ****, $p < 0.0001$;
1365 individual data points along with mean values \pm SD are depicted.

1366

1367 **Figure S6. Fc-mediated Antibody Effector Functions Contribute to *In Vivo* Efficacy of CV3-**
1368 **1 and CV3-25 During Prophylaxis. Related to Figure 6.**

1369 (A) A scheme showing experimental design for testing *in vivo* efficacy of NABs and their
1370 corresponding Leucine to Alanine (LALA) or G236A/S239D/A330L/I332E (GASDALIE) mutants
1371 (12.5 mg/kg body weight) delivered intraperitoneally (i.p.) 1 day before challenging K18-hACE2
1372 mice with 1×10^5 FFU of SARS-CoV-2 nLuc. Human IgG1-treated (12.5 mg/kg body weight) mice
1373 were used as control (Iso). Mice were followed by non-invasive BLI every 2 days from the start of
1374 infection using IVIS Spectrum after retroorbital administration of furimazine (nLuc substrate).
1375 (B) SARS-CoV-2 replication and dissemination in K18-hACE2 transgenic mice (n = 4-8 per group)
1376 for experiment as in A, were monitored via BLI in ventral (v) and dorsal (d) positions at the
1377 indicated days post infection every 2 days. The mice were euthanized on indicated days and
1378 imaged again after necropsy. Images from one representative experiment are shown.
1379 (C-D) A plot showing temporal quantification of nLuc signal acquired non-invasively and displayed
1380 as Flux (photons/sec) in whole body or brain region of SARS-CoV2-nLuc infected K18-hACE2
1381 mice for an experiment as in A. Each curve represents luminescent signal computed for individual
1382 mouse.
1383 (E) A plot showing temporal body weight changes of K18-hACE2 mice at indicated days post
1384 infection for an experiment shown in A. Each curve represents one animal. The body weight at
1385 the start of the experiment was set to 100%.
1386 (F) Kaplan-Meier survival curves of mice statistically compared by log-rank (Mantel-Cox) test for
1387 experiment as in A.
1388 (G) Plot showing viral loads as nLuc activity/mg of indicated organs using Vero E6 cells as targets.
1389 NLuc activity was determined 24 h after infection. Undetectable virus amounts were set to 1 for
1390 display on log plots.
1391 (H, I) A plot showing mRNA levels of indicated cytokines from lung and brain tissues of K18-
1392 hACE2 mice at the time of euthanasia as shown in F. The mRNA amounts were normalized to
1393 the levels seen in uninfected mice and the house keeping *Gapdh* mRNA.

1394 (J) A scheme showing experimental design for testing *in vivo* efficacy of CV3-1 and its
1395 corresponding Leucine to Alanine (LALA) mutant (12.5 mg/kg body weight) delivered
1396 intraperitoneally (i.p.) 1 day before challenging 12-14 weeks old C57BL/6 (B6) mice with 5×10^5
1397 FFU of mouse-adapted SARS-CoV-2 MA10. Human IgG1-treated (12.5 mg/kg body weight) mice
1398 were used as control (Iso).

1399 (K) A plot showing temporal body weight changes of B6 mice at indicated days post infection for
1400 an experiment shown in J. Each curve represents one animal. The body weight at the start of the
1401 experiment was set to 100%.

1402 (L) Kaplan-Meier survival curves of mice statistically compared by log-rank (Mantel-Cox) test for
1403 experiment as in A.

1404 (M-O) A plot showing fold changes in mRNA levels of I SARS-CoV-2 N or indicated cytokines
1405 from specified tissues of B6 mice at 7 dpi for an experiment as in J. The mRNA amounts were
1406 normalized to the levels seen in uninfected mice and the house keeping *Gapdh* mRNA.

1407 Scale bars in (B) denote radiance (photons/sec/cm²/steradian). Grouped data in (C-E) and (G-I),
1408 were analyzed by 2-way ANOVA followed by Dunnett's or Tukey's multiple comparison tests. The
1409 data in (K) and (M-O) were analyzed using unpaired Mann-Whitney test. Statistical significance:
1410 group comparisons to isotype control are shown in black; group comparisons between CV3-25
1411 LALA to CV3-25 and CV3-25 GASDALIE-treated cohorts are shown in red; group comparison
1412 between CV3-1 LALA and CV3-1 treated cohorts are shown in purple. *, $p < 0.05$; **, $p < 0.01$;
1413 ***, $p < 0.001$; ****, $p < 0.0001$; Mean values \pm SD are depicted.

1414

1415 **Figure S7. NK Cells Contribute Marginally to *In Vivo* Efficacy During CV3-1 Prophylaxis.**

1416 **Related to Figure 7.**

1417 (A) A scheme showing experimental design for testing the contribution of NK cells in K18-hACE2
1418 mice pretreated with CV3-1 NAb (i.p., 12.5 mg/kg body weight), 1 day before challenging with 1

1419 $\times 10^5$ FFU of SARS-CoV-2 nLuc. α NK1.1 mAb (i.p., 20 mg/kg body weight) was used to deplete
1420 NK cells at indicated time points. Corresponding human (for CV3-1) and rat (for α NK1.1)
1421 antibodies served as non-specific isotype controls. The mice were followed by non-invasive BLI
1422 every 2 days from the start of infection using IVIS Spectrum after retroorbital administration of
1423 furimazine (nLuc substrate).

1424 (B) SARS-CoV-2 replication and dissemination in indicated groups of K18-hACE2 transgenic mice
1425 ($n = 5$ per group) for experiment as in A, were monitored via BLI at ventral (v) and dorsal (d)
1426 positions at the indicated days post infection every 2 days. The mice were euthanized at indicated
1427 times and imaged again after necropsy. Images from one representative experiment are shown.

1428 (C-D) A plot showing temporal quantification of nLuc signal acquired non-invasively and displayed
1429 as photon flux (photons/sec) in whole body or brain region of SARS-CoV2-nLuc infected K18-
1430 hACE2 mice for an experiment as in A. Each curve represents luminescent signal computed for
1431 individual mouse. Scale bars denote radiance (photons/sec/cm²/steradian).

1432 (E) A plot showing temporal body weight changes in designated groups of K18-hACE2 mice at
1433 indicated days post infection for an experiment shown in A. Each curve represents one animal.
1434 The body weight at the start of the experiment was set to 100%.

1435 (F) Kaplan-Meier survival curves of mice statistically compared by log-rank (Mantel-Cox) test for
1436 experiment as in A.

1437 (G) Plot showing viral loads as nLuc activity/mg of indicated organs using Vero E6 cells as targets.
1438 Nluc activity was determined 24 h after infection. Undetectable virus amounts were set to 1 for
1439 display on log plots.

1440 (H, I) A plot showing mRNA levels of indicated cytokines from lung and brain tissues of K18-
1441 hACE2 mice at the time of euthanasia as shown in F. The mRNA amounts were normalized to
1442 the levels seen in uninfected mice and the house keeping gene GAPDH.

1443 (J, K) Representative FACS plots showing the gating strategy to identify NK cells (CD3⁺NK1.1⁺)
1444 and quantification to ascertain their depletion in PBMCs of indicated groups of mice.

1445 (L, M) Representative FACS plots showing the gating strategy to identify neutrophils cells (CD45⁺
1446 CD11b⁺Ly6G⁺) and quantification to ascertain their depletion in PBMCs of indicated groups of
1447 mice.

1448 (N, O) Representative FACS plots showing the gating strategy to identify Ly6C^{hi} monocytes and
1449 quantification to ascertain their depletion in PBMCs of indicated groups of mice.

1450 Grouped data in (C)-(E) and (G)-(I) were analyzed by 2-way ANOVA followed by Dunnett's or
1451 Tukey's multiple comparison tests. Statistical significance: group comparisons to isotype control
1452 are shown in black; group comparisons to Iso⁺CV3-1 treated cohort are in red. Pairwise
1453 comparisons in (K), (M) and (O) were analyzed using non-parametric Mann-Whitney test. *, $p <$
1454 0.05; **, $p < 0.01$; ***, $p < 0.001$; ****, $p < 0.0001$; Mean values \pm SD are depicted.

1455

1456 **Supplementary Table Legends:**

1457 **Table S1. A Comparison of SARS-CoV-2 Nucleocapsid (N) and *hACE2* mRNA Levels in K18-
1458 *hACE2* Mice Across Various Organs, Related to Figure 1 and S1**

1459 *p* values obtained by non-parametric Mann-Whitney test for pairwise comparison

1460

1461 **Supplementary Multimedia Files:**

1462 **Video S1. Longitudinal Non-invasive BLI of SARS-CoV-2-nLuc Infection and Dissemination
1463 in K18-hACE2 Mice, Related to Figure 1.**

1464 SARS-CoV-2-nLuc challenged mice were imaged daily in dorsal (d) and ventral (v) positions for
1465 6 days using IVIS Spectrum to monitor virus spread in the whole body as well as neuroinvasion.

1466

1467 **Video S2. Tomographic Reconstruction of SARS-CoV-2 Infected Lung Tissue, Related to
1468 Figure S2, panels B-D.**

1469 Virus particles are found within membrane-enclosed exit compartments of two adjacent
1470 pulmonary capillary endothelial cells. The movie traverses the reconstructed volume to illustrate
1471 the compartments (red arrowheads) then increases in magnification to detail the virions within the
1472 compartments.

1473 **Video S3. Cellular Overview and Tomogram of SARS-CoV-2 Infected Region in Lung**
1474 **Tissue, Related to Figure S2, panels B-D.**

1475 SARS-CoV-2 virions are found in regions containing identifiable immune cells. Movie begins with
1476 a large-field montaged overview, highlighting alveolar macrophages (blue), AT2 cells (green),
1477 AT1 cells (yellow) and pulmonary blood veins (red). The upper of two blood veins is detailed at
1478 higher magnification, showing 3 red blood cells (rbc) and the surrounding capillary endothelium.
1479 A region containing portions of two endothelial cells is selected for tomographic reconstruction,
1480 showing caveolae at the cell surfaces and localizing SARS-CoV-2 virions within cytoplasmic exit
1481 compartments.

1482

1483 **Video S4. Tomographic Reconstruction of SARS-CoV-2 Infected Brain Tissue, Related to**
1484 **Figure S2, panel F.**

1485 Virus particles are found within neurons, often appearing in linear groups within compartments
1486 bordering the edges of neuronal projections. The movie details the distinction between
1487 presumptive SARS-CoV-2 virions and typical synaptic neurotransmitter vesicles found in an
1488 adjacent synaptic terminal.

1489

1490 **Video S5. Tomographic Reconstruction of SARS-CoV-2 Infected Testis Tissue, Related to**
1491 **Figure S2, panel M.**

1492 Virus particles are found within membrane-enclosed compartments of Sertoli cells. Additional
1493 material and structures coexist with the virions in these compartments, suggesting they may be

1494 defined as lysosomes. Presumptive SARS-CoV-2 virions can be discerned from the other
1495 structures.

1496 **References**

- 1497 Alsoussi, W.B., Turner, J.S., Case, J.B., Zhao, H., Schmitz, A.J., Zhou, J.Q., Chen, R.E., Lei, T.,
1498 Rizk, A.A., McIntire, K.M., *et al.* (2020). A Potently Neutralizing Antibody Protects Mice against
1499 SARS-CoV-2 Infection. *J Immunol* 205, 915-922.
1500
1501 Amanat, F., White, K.M., Miorin, L., Strohmeier, S., McMahon, M., Meade, P., Liu, W.C., Albrecht,
1502 R.A., Simon, V., Martinez-Sobrido, L., *et al.* (2020). An In Vitro Microneutralization Assay for
1503 SARS-CoV-2 Serology and Drug Screening. *Curr Protoc Microbiol* 58, e108.
1504
1505 Anand, S.P., Prevost, J., Nayrac, M., Beaudoin-Bussieres, G., Benlarbi, M., Gasser, R., Brassard,
1506 N., Laumaea, A., Gong, S.Y., Bourassa, C., *et al.* (2021a). Longitudinal analysis of humoral
1507 immunity against SARS-CoV-2 Spike in convalescent individuals up to 8 months post-symptom
1508 onset. *bioRxiv* 2021.01.25.428097.
1509
1510 Anand, S.P., Prevost, J., Richard, J., Perreault, J., Tremblay, T., Drouin, M., Fournier, M.J., Lewin,
1511 A., Bazin, R., and Finzi, A. (2021b). High-throughput detection of antibodies targeting the SARS-
1512 CoV-2 Spike in longitudinal convalescent plasma samples. *Transfusion* 10.1111/trf.16318.
1513
1514 Baum, A., Ajithdoss, D., Copin, R., Zhou, A., Lanza, K., Negron, N., Ni, M., Wei, Y., Mohammadi,
1515 K., Musser, B., *et al.* (2020). REGN-COV2 antibodies prevent and treat SARS-CoV-2 infection in
1516 rhesus macaques and hamsters. *Science* 370, 1110-1115.
1517
1518 Beaudoin-Bussieres, G., Laumaea, A., Anand, S.P., Prevost, J., Gasser, R., Goyette, G.,
1519 Medjahed, H., Perreault, J., Tremblay, T., Lewin, A., *et al.* (2020). Decline of Humoral Responses
1520 against SARS-CoV-2 Spike in Convalescent Individuals. *mBio* 11, 10.1128/mBio.02590-02520.
1521
1522 Bolles, M., Deming, D., Long, K., Agnihothram, S., Whitmore, A., Ferris, M., Funkhouser, W.,
1523 Gralinski, L., Totura, A., and Heise, M. (2011). A double-inactivated severe acute respiratory
1524 syndrome coronavirus vaccine provides incomplete protection in mice and induces increased
1525 eosinophilic proinflammatory pulmonary response upon challenge. *Journal of virology* 85, 12201-
1526 12215.
1527
1528 Bournazos, S., DiLillo, D.J., Goff, A.J., Glass, P.J., and Ravetch, J.V. (2019). Differential
1529 requirements for FcγR engagement by protective antibodies against Ebola virus. *Proceedings of*
1530 *the National Academy of Sciences* 116, 20054-20062.
1531
1532 Bournazos, S., Klein, F., Pietzsch, J., Seaman, M.S., Nussenzweig, M.C., and Ravetch, J.V.
1533 (2014). Broadly neutralizing anti-HIV-1 antibodies require Fc effector functions for in vivo activity.
1534 *Cell* 158, 1243-1253.
1535
1536 Calomeni, E., Satoskar, A., Ayoub, I., Brodsky, S., Rovin, B.H., and Nadasdy, T. (2020).
1537 Multivesicular bodies mimicking SARS-CoV-2 in patients without COVID-19. *Kidney Int* 98, 233-
1538 234.
1539
1540 Carossino, M., Montanaro, P., O'Connell, A., Kenney, D., Gertje, H., Grosz, K.A., Kurnick, S.A.,
1541 Bosmann, M., Saeed, M., Balasuriya, U.B.R., *et al.* (2021). Fatal neuroinvasion of SARS-CoV-2
1542 in K18-hACE2 mice is partially dependent on hACE2 expression. *bioRxiv*,
1543 2021.2001.2013.425144.

- 1544 Chen, P., Nirula, A., Heller, B., Gottlieb, R.L., Boscia, J., Morris, J., Huhn, G., Cardona, J.,
1545 Mocherla, B., Stosor, V., *et al.* (2021). SARS-CoV-2 Neutralizing Antibody LY-CoV555 in
1546 Outpatients with Covid-19. *N Engl J Med* **384**, 229-237.
1547
1548 Cohen, A.A., Gnanapragasam, P.N.P., Lee, Y.E., Hoffman, P.R., Ou, S., Kakutani, L.M., Keeffe,
1549 J.R., Wu, H.J., Howarth, M., West, A.P., *et al.* (2021). Mosaic nanoparticles elicit cross-reactive
1550 immune responses to zoonotic coronaviruses in mice. *Science* **371**, 735-741.
1551
1552 Dinnon, K.H., 3rd, Leist, S.R., Schafer, A., Edwards, C.E., Martinez, D.R., Montgomery, S.A.,
1553 West, A., Yount, B.L., Jr., Hou, Y.J., Adams, L.E., *et al.* (2020). A mouse-adapted model of SARS-
1554 CoV-2 to test COVID-19 countermeasures. *Nature* **586**, 560-566.
1555
1556 Dekkers, G., Bentlage, A.E.H., Stegmann, T.C., Howie, H.L., Lissenberg-Thunnissen, S., Zimring,
1557 J., Rispens, T., and Vidarsson, G. (2017). Affinity of human IgG subclasses to mouse Fc gamma
1558 receptors. *MAbs* **9**, 767-773.
1559
1560 Del Valle, D.M., Kim-Schulze, S., Huang, H.H., Beckmann, N.D., Nirenberg, S., Wang, B., Lavin,
1561 Y., Swartz, T.H., Madduri, D., Stock, A., *et al.* (2020). An inflammatory cytokine signature predicts
1562 COVID-19 severity and survival. *Nat Med* **26**, 1636-1643.
1563
1564 DiLillo, D.J., Tan, G.S., Palese, P., and Ravetch, J.V. (2014). Broadly neutralizing hemagglutinin
1565 stalk-specific antibodies require FcγR interactions for protection against influenza virus in vivo.
1566 *Nature medicine* **20**, 143-151.
1567
1568 Ding, S., Laumaea, A., Benlarbi, M., Beaudoin-Bussieres, G., Gasser, R., Medjahed, H., Pancera,
1569 M., Stamatatos, L., McGuire, A.T., Bazin, R., *et al.* (2020). Antibody Binding to SARS-CoV-2 S
1570 Glycoprotein Correlates with but Does Not Predict Neutralization. *Viruses* **12**,
1571 10.1101/2020.1109.1108.287482.
1572
1573 Ellul, M.A., Benjamin, L., Singh, B., Lant, S., Michael, B.D., Easton, A., Kneen, R., Defres, S.,
1574 Sejvar, J., and Solomon, T. (2020). Neurological associations of COVID-19. *Lancet Neurol* **19**,
1575 767-783.
1576
1577 Fagre, A.C., Manhard, J., Adams, R., Eckley, M., Zhan, S., Lewis, J., Rocha, S.M., Woods, C.,
1578 Kuo, K., and Liao, W. (2020). A potent SARS-CoV-2 neutralizing human monoclonal antibody that
1579 reduces viral burden and disease severity in Syrian hamsters. *Frontiers in immunology* **11**,
1580 10.3389/fimmu.2020.614256.
1581
1582 Falzarano, D., Groseth, A., and Hoenen, T. (2014). Development and application of reporter-
1583 expressing mononegaviruses: current challenges and perspectives. *Antiviral Res* **103**, 78-87.
1584
1585 Finzi, A., Xiang, S.H., Pacheco, B., Wang, L., Haight, J., Kassa, A., Danek, B., Pancera, M.,
1586 Kwong, P.D., and Sodroski, J. (2010). Topological layers in the HIV-1 gp120 inner domain
1587 regulate gp41 interaction and CD4-triggered conformational transitions. *Mol Cell* **37**, 656-667.
1588
1589 Golden, J., Cline, C., Zeng, X., Garrison, A., Carey, B., Mucker, E., White, L., Shamblin, J.,
1590 Brocato, R., and Liu, J. (2020). Human angiotensin-converting enzyme 2 transgenic mice infected
1591 with SARS-CoV-2 develop severe and fatal respiratory disease. *JCI Insight*
1592 *10.1172/jci.insight.142032*.
1593

- 1594 Gorman, M.J., Patel, N., Guebre-Xabier, M., Zhu, A., Atyeo, C., Pullen, K.M., Loos, C., Goez-
1595 Gazi, Y., Carrion, R., Tian, J.-H., *et al.* (2021). Collaboration between the Fab and Fc contribute
1596 to maximal protection against SARS-CoV-2 in nonhuman primates following NVX-CoV2373
1597 subunit vaccine with Matrix-M™ vaccination. *bioRxiv*, 2021.2002.2005.429759.
1598
1599 Graham, R.L., and Baric, R.S. (2020). SARS-CoV-2: Combating Coronavirus Emergence.
1600 *Immunity* 52, 734-736.
1601
1602 Halstead, S.B., and Katzelnick, L. (2020). COVID-19 Vaccines: Should We Fear ADE? *The*
1603 *Journal of infectious diseases* 222, 1946-1950.
1604
1605 Hansen, J., Baum, A., Pascal, K.E., Russo, V., Giordano, S., Wloga, E., Fulton, B.O., Yan, Y.,
1606 Koon, K., and Patel, K. (2020). Studies in humanized mice and convalescent humans yield a
1607 SARS-CoV-2 antibody cocktail. *Science* 369, 1010-1014.
1608
1609 Hassan, A.O., Case, J.B., Winkler, E.S., Thackray, L.B., Kafai, N.M., Bailey, A.L., McCune, B.T.,
1610 Fox, J.M., Chen, R.E., Alsoussi, W.B., *et al.* (2020). A SARS-CoV-2 Infection Model in Mice
1611 Demonstrates Protection by Neutralizing Antibodies. *Cell* 182, 744-753 e744.
1612
1613 He, W., Ladinsky, M.S., Huey-Tubman, K.E., Jensen, G.J., McIntosh, J.R., and Bjorkman, P.J.
1614 (2008). FcRn-mediated antibody transport across epithelial cells revealed by electron
1615 tomography. *Nature* 455, 542-546.
1616
1617 Hoffmann, M., Kleine-Weber, H., Schroeder, S., Kruger, N., Herrler, T., Erichsen, S., Schiergens,
1618 T.S., Herrler, G., Wu, N.H., Nitsche, A., *et al.* (2020). SARS-CoV-2 Cell Entry Depends on ACE2
1619 and TMPRSS2 and Is Blocked by a Clinically Proven Protease Inhibitor. *Cell* 181, 271-280 e278.
1620
1621 Hoffmann, M., Muller, M.A., Drexler, J.F., Glende, J., Erdt, M., Gutzkow, T., Losemann, C., Binger,
1622 T., Deng, H., Schwegmann-Wessels, C., *et al.* (2013). Differential sensitivity of bat cells to
1623 infection by enveloped RNA viruses: coronaviruses, paramyxoviruses, filoviruses, and influenza
1624 viruses. *PLoS One* 8, e72942.
1625
1626 Hofmann, H., Pyrc, K., van der Hoek, L., Geier, M., Berkhout, B., and Pohlmann, S. (2005).
1627 Human coronavirus NL63 employs the severe acute respiratory syndrome coronavirus receptor
1628 for cellular entry. *Proc Natl Acad Sci U S A* 102, 7988-7993.
1629
1630 Hsieh, C.L., Goldsmith, J.A., Schaub, J.M., DiVenere, A.M., Kuo, H.C., Javanmardi, K., Le, K.C.,
1631 Wrapp, D., Lee, A.G., Liu, Y., *et al.* (2020). Structure-based design of prefusion-stabilized SARS-
1632 CoV-2 spikes. *Science* 369, 1501-1505.
1633
1634 Iwasaki, A., and Yang, Y. (2020). The potential danger of suboptimal antibody responses in
1635 COVID-19. *Nat Rev Immunol* 20, 339-341.
1636
1637 Jennewein, M.F., MacCamy, A.J., Akins, N.R., Feng, J., Homad, L.J., Hurlburt, N.K., Seydoux,
1638 E., Wan, Y.H., Stuart, A.B., Edara, V.V., *et al.* (2021). Isolation and Characterization of Cross-
1639 Neutralizing Coronavirus Antibodies from COVID-19+ Subjects. *bioRxiv* 2021,
1640 10.1101/2021.03.23.436684
1641
1642 Johansen, M.D., Irving, A., Montagutelli, X., Tate, M.D., Rudloff, I., Nold, M.F., Hansbro, N.G.,
1643 Kim, R.Y., Donovan, C., Liu, G., *et al.* (2020). Animal and translational models of SARS-CoV-2
1644 infection and COVID-19. *Mucosal Immunol* 13, 877-891.

1645
1646 Juette, M.F., Terry, D.S., Wasserman, M.R., Altman, R.B., Zhou, Z., Zhao, H., and Blanchard,
1647 S.C. (2016). Single-molecule imaging of non-equilibrium molecular ensembles on the millisecond
1648 timescale. *Nat Methods* **13**, 341-344.
1649
1650 Ke, Z., Oton, J., Qu, K., Cortese, M., Zila, V., McKeane, L., Nakane, T., Zivanov, J., Neufeldt,
1651 C.J., Cerikan, B., *et al.* (2020). Structures and distributions of SARS-CoV-2 spike proteins on
1652 intact virions. *Nature* **588**, 498-502.
1653
1654 Klasse, P.J., and Moore, J.P. (2020). Antibodies to SARS-CoV-2 and their potential for
1655 therapeutic passive immunization. *Elife* **9**, 10.7554/eLife.57877.
1656
1657 Klein, S., Cortese, M., Winter, S.L., Wachsmuth-Melm, M., Neufeldt, C.J., Cerikan, B., Stanifer,
1658 M.L., Boulant, S., Bartenschlager, R., and Chlanda, P. (2020). SARS-CoV-2 structure and
1659 replication characterized by in situ cryo-electron tomography. *Nat Commun* **11**, 5885.
1660 Ladinsky, M.S., Huey-Tubman, K.E., and Bjorkman, P.J. (2012). Electron tomography of late
1661 stages of FcRn-mediated antibody transcytosis in neonatal rat small intestine. *Mol Biol Cell* **23**,
1662 2537-2545.
1663
1664 Leist, S.R., Dinnon, K.H., 3rd, Schafer, A., Tse, L.V., Okuda, K., Hou, Y.J., West, A., Edwards,
1665 C.E., Sanders, W., Fritch, E.J., *et al.* (2020a). A Mouse-Adapted SARS-CoV-2 Induces Acute
1666 Lung Injury and Mortality in Standard Laboratory Mice. *Cell* **183**, 1070-1085 e1012.
1667
1668 Leist, S.R., Schäfer, A., and Martinez, D.R. (2020b). Cell and animal models of SARS-CoV-2
1669 pathogenesis and immunity. *Disease Models & Mechanisms* **13**, dmm046581.
1670
1671 Li, D., Edwards, R.J., Manne, K., Martinez, D.R., Schäfer, A., Alam, S.M., Wiehe, K., Lu, X., Parks,
1672 R., Sutherland, L.L., *et al.* (2021). The functions of SARS-CoV-2 neutralizing and infection-
1673 enhancing antibodies in vitro and in mice and nonhuman primates. *bioRxiv*,
1674 2020.2012.2031.424729.
1675
1676 Li, W., Chen, C., Drelich, A., Martinez, D.R., Gralinski, L.E., Sun, Z., Schafer, A., Kulkarni, S.S.,
1677 Liu, X., Leist, S.R., *et al.* (2020). Rapid identification of a human antibody with high prophylactic
1678 and therapeutic efficacy in three animal models of SARS-CoV-2 infection. *Proc Natl Acad Sci U*
1679 *S A* **117**, 29832-29838.
1680
1681 Liu, L., Wang, P., Nair, M.S., Yu, J., Rapp, M., Wang, Q., Luo, Y., Chan, J.F., Sahi, V., Figueroa,
1682 A., *et al.* (2020). Potent neutralizing antibodies against multiple epitopes on SARS-CoV-2 spike.
1683 *Nature* **584**, 450-456.
1684
1685 Liu, Z., Pan, Q., Ding, S., Qian, J., Xu, F., Zhou, J., Cen, S., Guo, F., and Liang, C. (2013). The
1686 interferon-inducible MxB protein inhibits HIV-1 infection. *Cell Host Microbe* **14**, 398-410.
1687 Lu, L.L., Suscovich, T.J., Fortune, S.M., and Alter, G. (2018). Beyond binding: antibody effector
1688 functions in infectious diseases. *Nature Reviews Immunology* **18**, 46.
1689
1690 Lu, M., Ma, X., Castillo-Menendez, L.R., Gorman, J., Alshafi, N., Ermel, U., Terry, D.S.,
1691 Chambers, M., Peng, D., Zhang, B., *et al.* (2019). Associating HIV-1 envelope glycoprotein
1692 structures with states on the virus observed by smFRET. *Nature* **568**, 415-419.
1693

1694 Lu, M., Uchil, P.D., Li, W., Zheng, D., Terry, D.S., Gorman, J., Shi, W., Zhang, B., Zhou, T., Ding,
1695 S., *et al.* (2020). Real-Time Conformational Dynamics of SARS-CoV-2 Spikes on Virus Particles.
1696 *Cell Host Microbe* 28, 880-891 e888.
1697
1698 Mack, M., Cihak, J., Simonis, C., Luckow, B., Proudfoot, A.E., Plachý, J.í., Brühl, H., Frink, M.,
1699 Anders, H.-J., and Vielhauer, V. (2001). Expression and characterization of the chemokine
1700 receptors CCR2 and CCR5 in mice. *The Journal of Immunology* 166, 4697-4704.
1701
1702 Mastronarde, D.N. (2005). Automated electron microscope tomography using robust prediction
1703 of specimen movements. *J Struct Biol* 152, 36-51.
1704 Mastronarde, D.N. (2008). Correction for non-perpendicularity of beam and tilt axis in tomographic
1705 reconstructions with the IMOD package. *J Microsc* 230, 212-217.
1706
1707 Mastronarde, D.N., and Held, S.R. (2017). Automated tilt series alignment and tomographic
1708 reconstruction in IMOD. *J Struct Biol* 197, 102-113.
1709
1710 McCray, P.B., Pewe, L., Wohlford-Lenane, C., Hickey, M., Manzel, L., Shi, L., Netland, J., Jia,
1711 H.P., Halabi, C., and Sigmund, C.D. (2007). Lethal infection of K18-hACE2 mice infected with
1712 severe acute respiratory syndrome coronavirus. *Journal of virology* 81, 813-821.
1713
1714 Munro, J.B., Gorman, J., Ma, X., Zhou, Z., Arthos, J., Burton, D.R., Koff, W.C., Courter, J.R.,
1715 Smith, A.B., 3rd, Kwong, P.D., *et al.* (2014). Conformational dynamics of single HIV-1 envelope
1716 trimers on the surface of native virions. *Science* 346, 759-763.
1717
1718 Noy-Porat, T., Mechaly, A., Levy, Y., Makdasi, E., Alcalay, R., Gur, D., Aftalion, M., Falach, R.,
1719 Ben-Arye, S.L., Lazar, S., *et al.* (2021). Therapeutic antibodies, targeting the SARS-CoV-2 spike
1720 N-terminal domain, protect lethally infected K18-hACE2 mice. *bioRxiv*, 2021.2002.2002.428995.
1721
1722 Park, J.E., Li, K., Barlan, A., Fehr, A.R., Perlman, S., McCray, P.B., Jr., and Gallagher, T. (2016).
1723 Proteolytic processing of Middle East respiratory syndrome coronavirus spikes expands virus
1724 tropism. *Proc Natl Acad Sci U S A* 113, 12262-12267.
1725
1726 Prevost, J., Gasser, R., Beaudoin-Bussieres, G., Richard, J., Duerr, R., Laumaea, A., Anand,
1727 S.P., Goyette, G., Benlarbi, M., Ding, S., *et al.* (2020). Cross-Sectional Evaluation of Humoral
1728 Responses against SARS-CoV-2 Spike. *Cell Rep Med* 1, 100126.
1729
1730 Rogers, T.F., Zhao, F., Huang, D., Beutler, N., Burns, A., He, W.T., Limbo, O., Smith, C., Song,
1731 G., Woehl, J., *et al.* (2020). Isolation of potent SARS-CoV-2 neutralizing antibodies and protection
1732 from disease in a small animal model. *Science* 369, 956-963.
1733
1734 Ruckwardt, T.J., Morabito, K.M., and Graham, B.S. (2019). Immunological lessons from
1735 respiratory syncytial virus vaccine development. *Immunity* 51, 429-442.
1736
1737 Saunders, K.O. (2019). Conceptual Approaches to Modulating Antibody Effector Functions and
1738 Circulation Half-Life. *Front Immunol* 10, 1296.
1739
1740 Sauer, M.M., Tortorici, M.A., Park, Y.J., Walls, A.C., Homad, L., Acton, O.J., Bowen, J.E., Wang,
1741 C., Xiong, X., de van der Schueren, W., *et al.* (2021). Structural basis for broad coronavirus
1742 neutralization. *Nat Struct Mol Biol* 28, 478-486.
1743

1744 Schafer, A., Muecksch, F., Lorenzi, J.C.C., Leist, S.R., Cipolla, M., Bournazos, S., Schmidt, F.,
1745 Maison, R.M., Gazumyan, A., Martinez, D.R., *et al.* (2021). Antibody potency, effector function,
1746 and combinations in protection and therapy for SARS-CoV-2 infection in vivo. *J Exp Med* **218**,
1747 10.1084/jem.20201993.

1748
1749 Shi, P.Y., Plante, J., Liu, Y., Liu, J., Xia, H., Johnson, B., Lokugamage, K., Zhang, X., Muruato,
1750 A., Zou, J., *et al.* (2020a). Spike mutation D614G alters SARS-CoV-2 fitness and neutralization
1751 susceptibility. *Res Sq*, 10.21203/rs.21203.rs-70482/v21201.

1752
1753 Shi, R., Shan, C., Duan, X., Chen, Z., Liu, P., Song, J., Song, T., Bi, X., Han, C., and Wu, L.
1754 (2020b). A human neutralizing antibody targets the receptor-binding site of SARS-CoV-2. *Nature*
1755 **584**, 120-124.

1756
1757 Silvas, J., Morales-Vasquez, D., Park, J.-G., Chiem, K., Torrelles, J.B., Platt, R.N., Anderson, T.,
1758 Ye, C., and Martinez-Sobrido, L. (2021). Contribution of SARS-CoV-2 accessory proteins to viral
1759 pathogenicity in K18 hACE2 transgenic mice. *bioRxiv*, 2021.2003.2009.434696.

1760
1761 Smith, P., DiLillo, D.J., Bournazos, S., Li, F., and Ravetch, J.V. (2012). Mouse model
1762 recapitulating human Fcγ receptor structural and functional diversity. *Proceedings of the National*
1763 *Academy of Sciences* **109**, 6181-6186.

1764
1765 Stamatatos, L., Czartoski, J., Wan, Y.-H., Homad, L.J., Rubin, V., Glantz, H., Neradilek, M.,
1766 Seydoux, E., Jennewein, M.F., MacCamy, A.J., *et al.* (2021). Antibodies elicited by SARS-CoV-2
1767 infection and boosted by vaccination neutralize an emerging variant and SARS-CoV-1. *medRxiv*,
1768 2021.2002.2005.21251182.

1769
1770 ter Meulen, J., van den Brink, E.N., Poon, L.L., Marissen, W.E., Leung, C.S., Cox, F., Cheung,
1771 C.Y., Bakker, A.Q., Bogaards, J.A., van Deventer, E., *et al.* (2006). Human monoclonal antibody
1772 combination against SARS coronavirus: synergy and coverage of escape mutants. *PLoS Med* **3**,
1773 e237.

1774
1775 Tortorici, M.A., Beltramello, M., Lempp, F.A., Pinto, D., Dang, H.V., Rosen, L.E., McCallum, M.,
1776 Bowen, J., Minola, A., Jaconi, S., *et al.* (2020). Ultrapotent human antibodies protect against
1777 SARS-CoV-2 challenge via multiple mechanisms. *Science* **370**, 950-957.

1778
1779 Turonova, B., Sikora, M., Schurmann, C., Hagen, W.J.H., Welsch, S., Blanc, F.E.C., von Bulow,
1780 S., Gecht, M., Bagola, K., Horner, C., *et al.* (2020). In situ structural analysis of SARS-CoV-2
1781 spike reveals flexibility mediated by three hinges. *Science* **370**, 203-208.

1782
1783 Ventura, J.D., Beloor, J., Allen, E., Zhang, T., Haugh, K.A., Uchil, P.D., Ochsenbauer, C., Kieffer,
1784 C., Kumar, P., Hope, T.J., *et al.* (2019). Longitudinal bioluminescent imaging of HIV-1 infection
1785 during antiretroviral therapy and treatment interruption in humanized mice. *PLoS Pathog* **15**,
1786 e1008161.

1787
1788 Voss, W.N., Hou, Y.J., Johnson, N.V., Kim, J.E., Delidakis, G., Horton, A.P., Bartzoka, F., Paresi,
1789 C.J., Tanno, Y., Abbasi, S.A., *et al.* (2020). Prevalent, protective, and convergent IgG recognition
1790 of SARS-CoV-2 non-RBD spike epitopes in COVID-19 convalescent plasma. *bioRxiv*,
1791 10.1101/2020.1112.1120.423708.

1792

- 1793 Weinreich, D.M., Sivapalasingam, S., Norton, T., Ali, S., Gao, H., Bhore, R., Musser, B.J., Soo,
1794 Y., Rofail, D., Im, J., *et al.* (2021). REGN-COV2, a Neutralizing Antibody Cocktail, in Outpatients
1795 with Covid-19. *N Engl J Med* **384**, 238-251.
1796
- 1797 Winkler, E.S., Bailey, A.L., Kafai, N.M., Nair, S., McCune, B.T., Yu, J., Fox, J.M., Chen, R.E.,
1798 Earnest, J.T., and Keeler, S.P. (2020). SARS-CoV-2 infection of human ACE2-transgenic mice
1799 causes severe lung inflammation and impaired function. *Nature immunology* **21**, 1327-1335.
1800
- 1801 Winkler, E.S., Gilchuk, P., Yu, J., Bailey, A.L., Chen, R.E., Chong, Z., Zost, S.J., Jang, H., Huang,
1802 Y., Allen, J.D., *et al.* (2021). Human neutralizing antibodies against SARS-CoV-2 require intact
1803 Fc effector functions for optimal therapeutic protection. *Cell*, 10.1016/j.cell.2021.1002.1026.
1804
- 1805 Xie, X., Muruato, A., Lokugamage, K.G., Narayanan, K., Zhang, X., Zou, J., Liu, J., Schindewolf,
1806 C., Bopp, N.E., Aguilar, P.V., *et al.* (2020a). An Infectious cDNA Clone of SARS-CoV-2. *Cell Host*
1807 *Microbe* **27**, 841-848 e843.
1808
- 1809 Xie, X., Muruato, A.E., Zhang, X., Lokugamage, K.G., Fontes-Garfias, C.R., Zou, J., Liu, J., Ren,
1810 P., Balakrishnan, M., Cihlar, T., *et al.* (2020b). A nanoluciferase SARS-CoV-2 for rapid
1811 neutralization testing and screening of anti-infective drugs for COVID-19. *Nat Commun* **11**, 5214.
1812
- 1813 Yao, H., Song, Y., Chen, Y., Wu, N., Xu, J., Sun, C., Zhang, J., Weng, T., Zhang, Z., Wu, Z., *et*
1814 *al.* (2020). Molecular Architecture of the SARS-CoV-2 Virus. *Cell* **183**, 730-738 e713.
1815
- 1816 Zhang, L., Jackson, C.B., Mou, H., Ojha, A., Peng, H., Quinlan, B.D., Rangarajan, E.S., Pan, A.,
1817 Vanderheiden, A., Suthar, M.S., *et al.* (2020). SARS-CoV-2 spike-protein D614G mutation
1818 increases virion spike density and infectivity. *Nat Commun* **11**, 10.1038/s41467-41020-19808-
1819 41464.
1820
- 1821 Zost, S.J., Gilchuk, P., Case, J.B., Binshtein, E., Chen, R.E., Nkolola, J.P., Schäfer, A., Reidy,
1822 J.X., Trivette, A., and Nargi, R.S. (2020a). Potently neutralizing and protective human antibodies
1823 against SARS-CoV-2. *Nature* **584**, 443-449.
1824
- 1825 Zost, S.J., Gilchuk, P., Chen, R.E., Case, J.B., Reidy, J.X., Trivette, A., Nargi, R.S., Sutton, R.E.,
1826 Suryadevara, N., and Chen, E.C. (2020b). Rapid isolation and profiling of a diverse panel of
1827 human monoclonal antibodies targeting the SARS-CoV-2 spike protein. *Nature medicine* **26**,
1828 1422-1427.

Figure 1

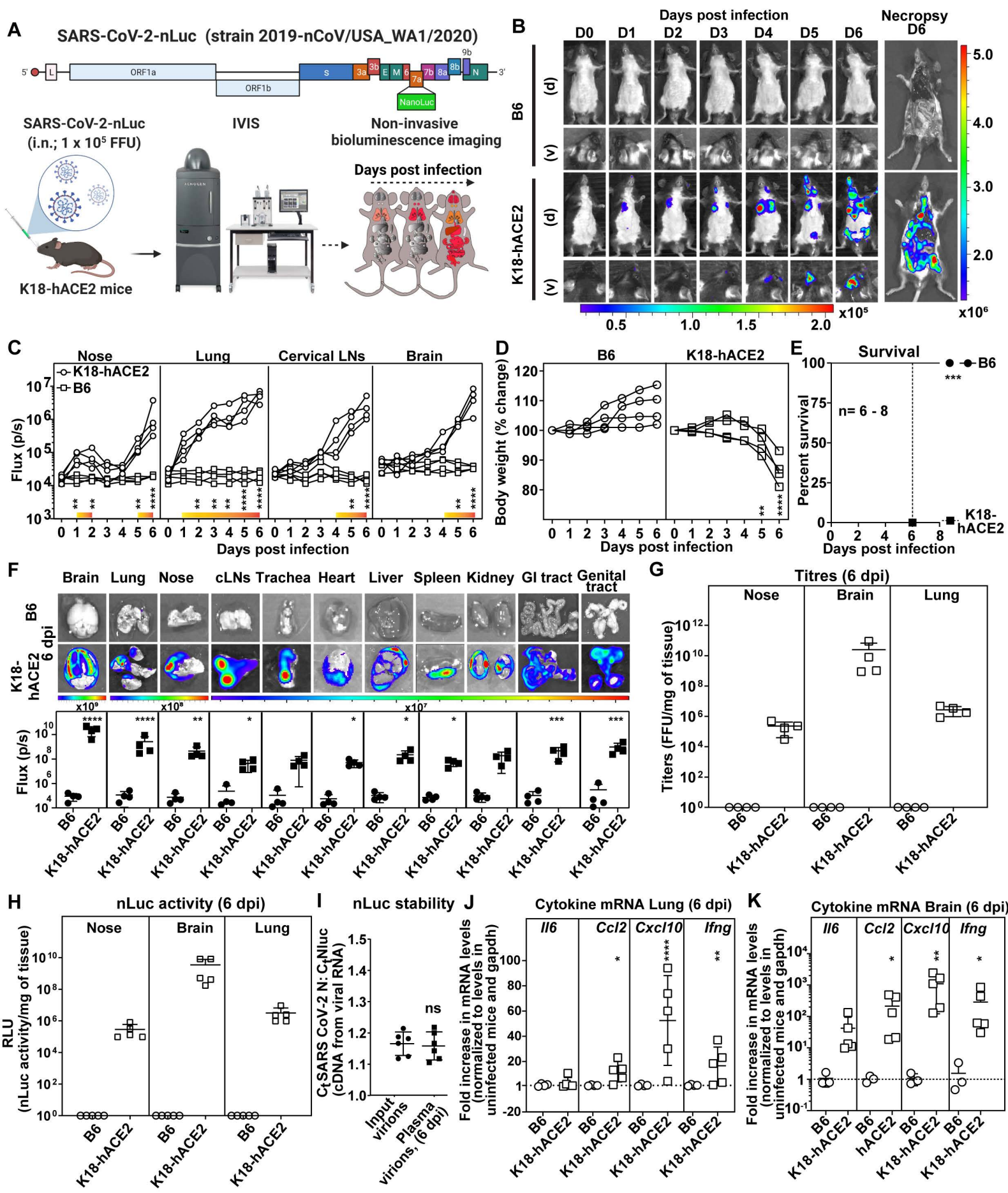


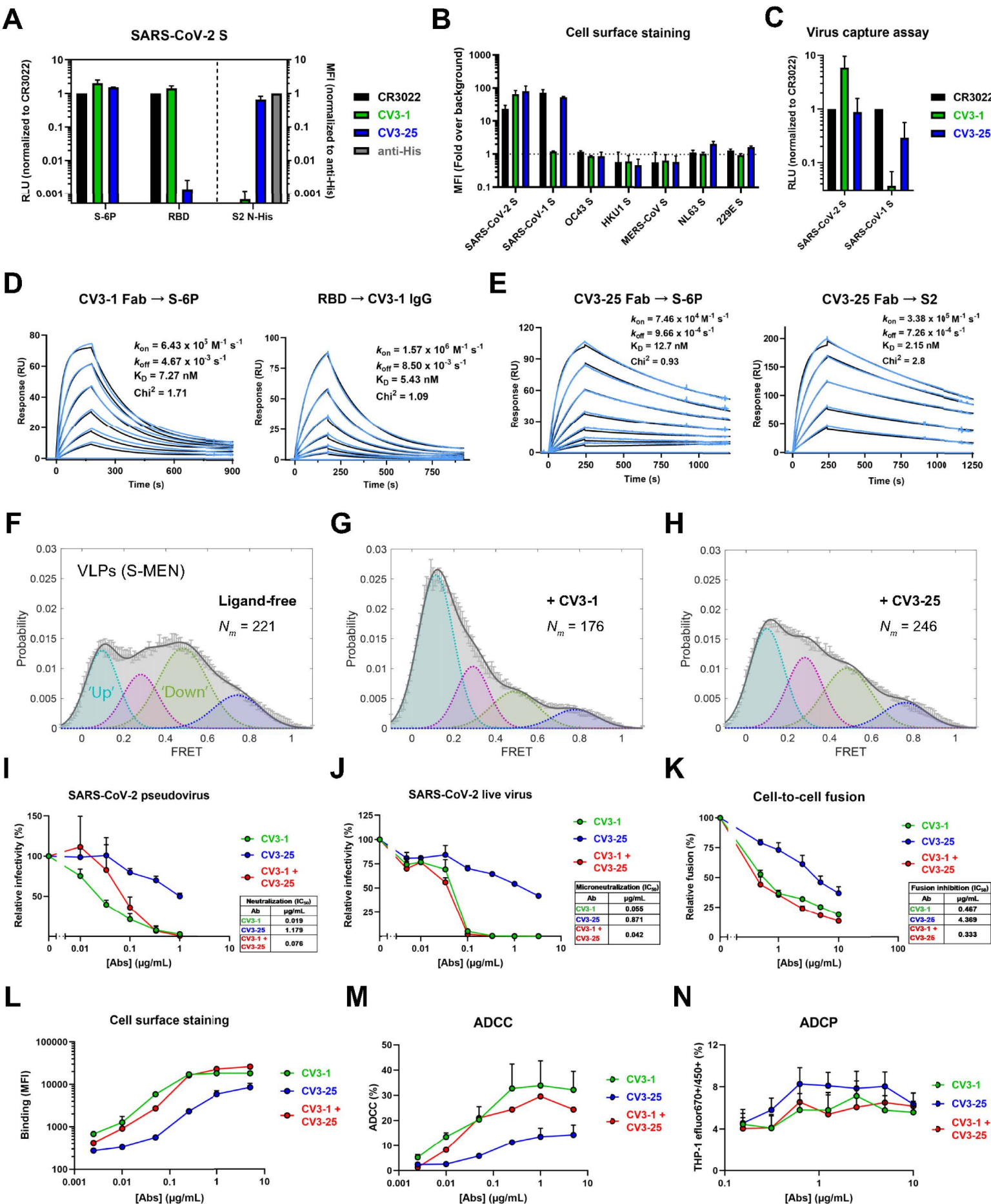
Figure 3

Figure 4

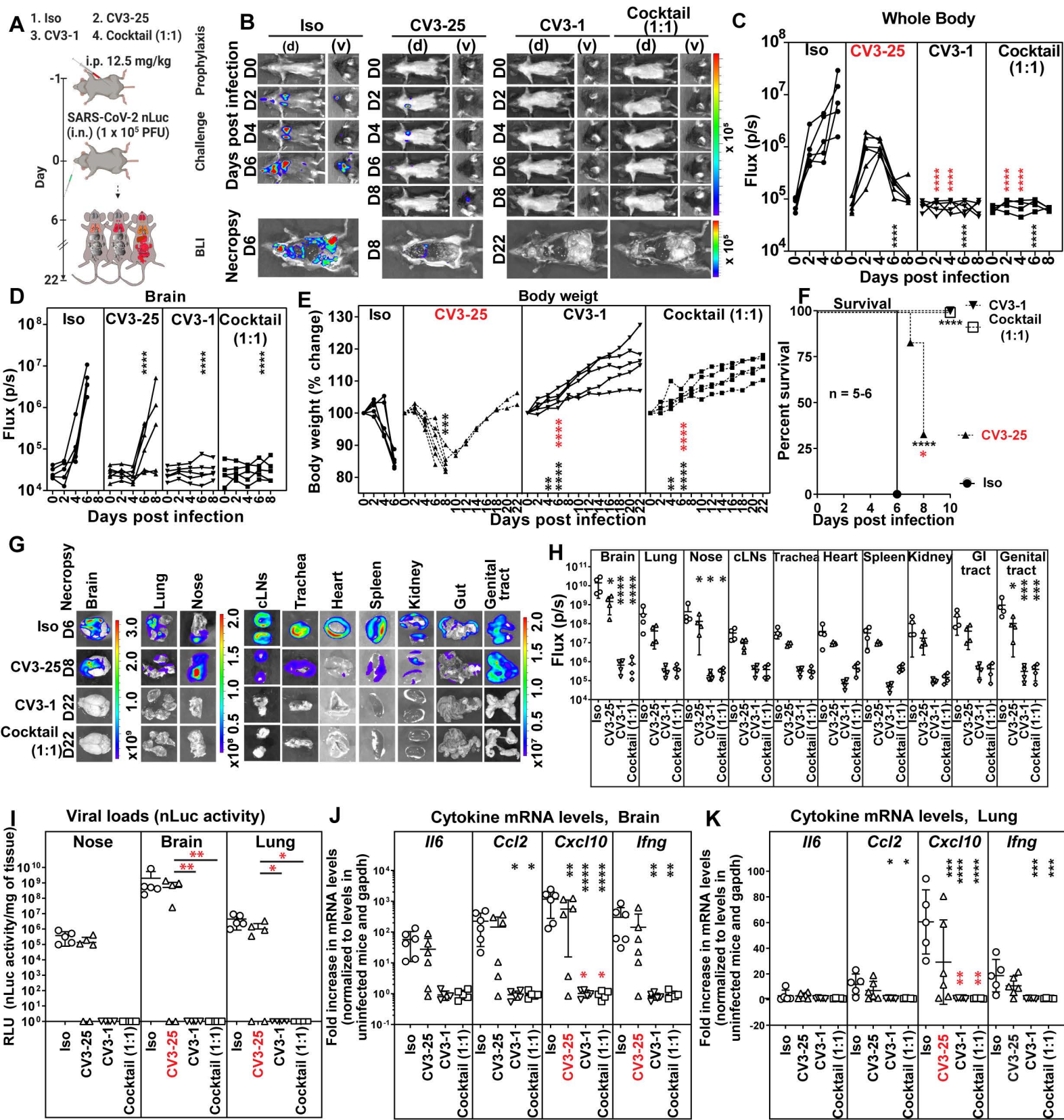


Figure 5

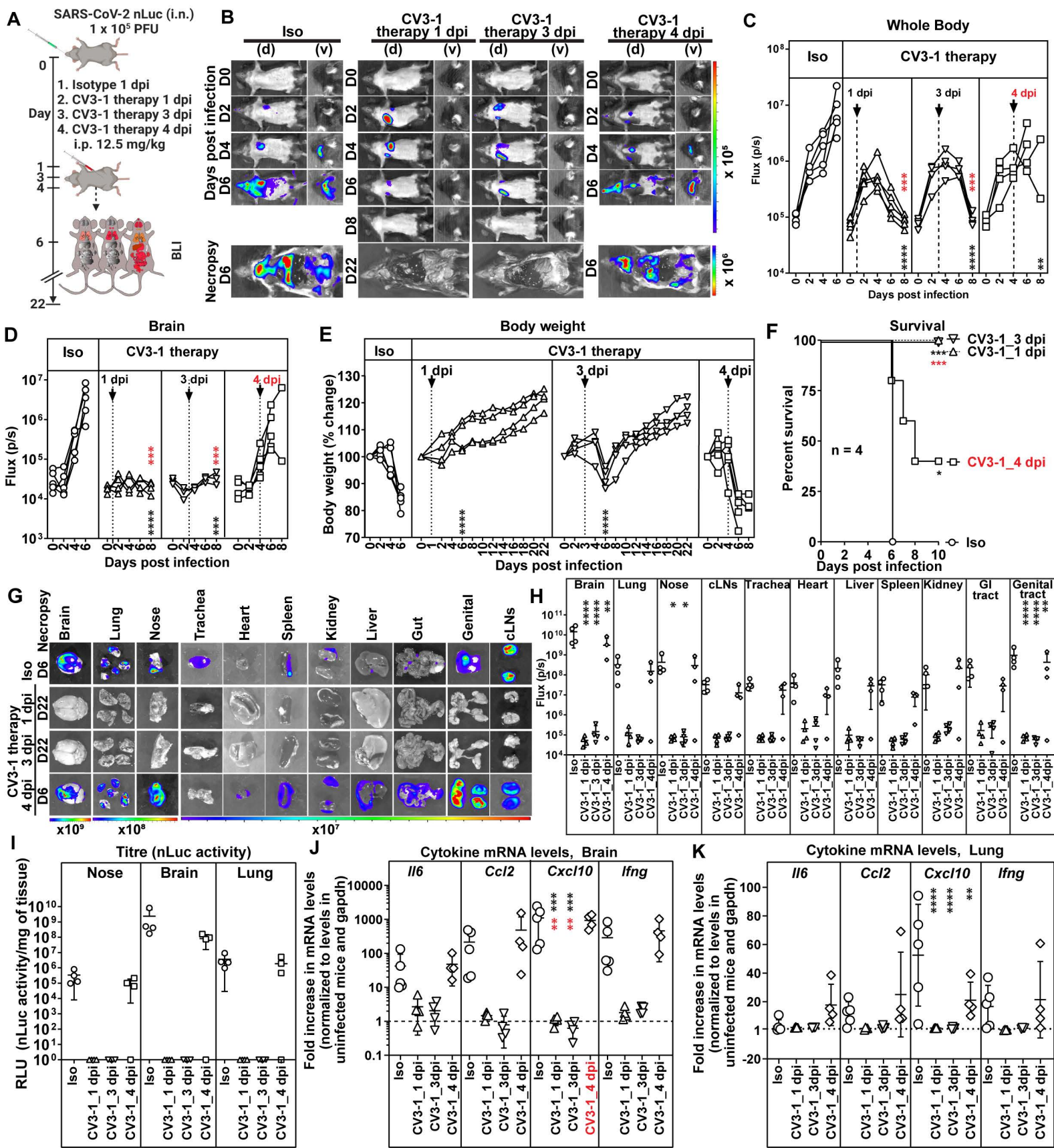


Figure 6

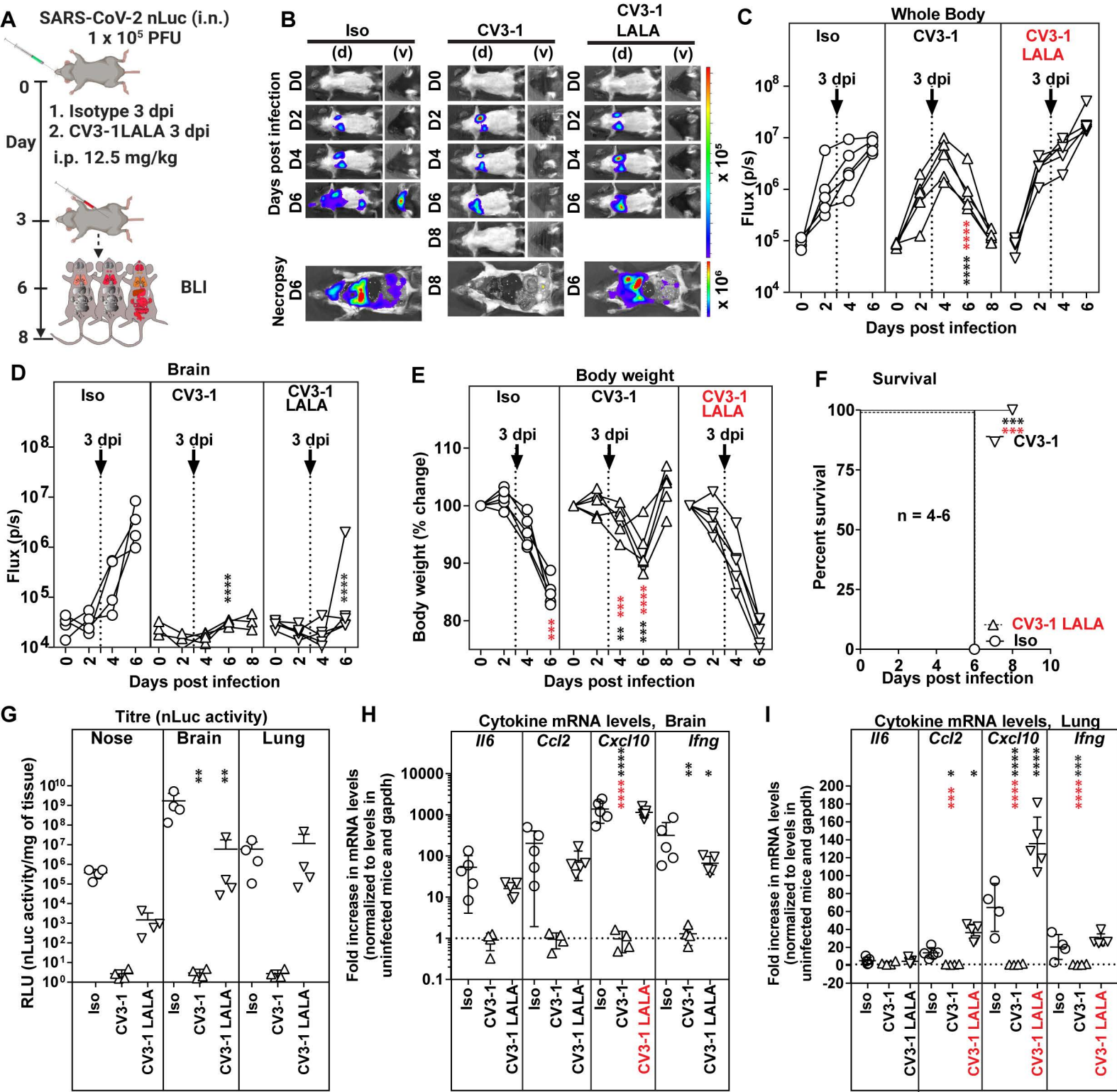


Figure 7

